



**HAL**  
open science

# Eruptive history of the Late Quaternary Ciomadul (Csomád) volcano, East Carpathians, Part I: Timing of lava dome activity

P. Lahitte, S. Dibacto, D. Karátson, R. Gertisser, D. Veres

► **To cite this version:**

P. Lahitte, S. Dibacto, D. Karátson, R. Gertisser, D. Veres. Eruptive history of the Late Quaternary Ciomadul (Csomád) volcano, East Carpathians, Part I: Timing of lava dome activity. *Bulletin of Volcanology*, 2019, 81 (4), pp.27. 10.1007/s00445-019-1286-9 . hal-04420575

**HAL Id: hal-04420575**

**<https://hal.science/hal-04420575>**

Submitted on 26 Jan 2024

**HAL** is a multi-disciplinary open access archive for the deposit and dissemination of scientific research documents, whether they are published or not. The documents may come from teaching and research institutions in France or abroad, or from public or private research centers.

L'archive ouverte pluridisciplinaire **HAL**, est destinée au dépôt et à la diffusion de documents scientifiques de niveau recherche, publiés ou non, émanant des établissements d'enseignement et de recherche français ou étrangers, des laboratoires publics ou privés.

[Click here to view linked References](#)

# 1 **Eruptive history of the Late Quaternary Ciomadul (Csomád) volcano,**

## 2 **East Carpathians, Part I: Timing of lava dome activity**

3 **Lahitte, P.<sup>1</sup>, Dibacto, S.<sup>1</sup>, Karátson, D.<sup>2</sup>, Gertisser, R.<sup>3</sup>, Veres, D.<sup>4</sup>**

4 1: GEOPS, Univ. Paris-Sud, CNRS, Université Paris-Saclay, Rue du Belvédère, Bât. 504, 91405

5 Orsay, France

6 2: Eötvös University, Department of Physical Geography, H-1117 Budapest, Pázmány s. 1/C,

7 Hungary

8 3: School of Geography, Geology and the Environment, Keele University, Keele, ST5 5BG, UK

9 4: Romanian Academy, Institute of Speleology, Clinicilor 5, 400006 Cluj-Napoca, Romania

### 10 **Abstract**

11 Located at the southern tip of the Intra-Carpathian Volcanic Range in Romania, and  
12 composed of a dozen dacitic lava domes, the Ciomadul (Csomád) volcanic complex is the  
13 youngest eruptive centre of the Carpatho-Pannonian Region. Whereas, in the last decade,  
14 the explosive history of Ciomadul since 50 ka has been well constrained by numerous  
15 studies, the chronology of the dome sequence still lacks robust chronological constraints and  
16 an extended analysis of all available data. Here, we apply a detailed K-Ar dating approach to  
17 refine the chronology of the lava dome eruptions, using the unspiked K-Ar Cassinot-Gillot  
18 technique. Our dating focused on the most voluminous central part of the lava dome  
19 complex. New eruption ages were determined following a strict separation (of 10 g) of  
20 groundmass from about 3 kg of unaltered sample rocks, thereby isolating material whose

21 cooling was contemporaneous with the eruption. The newly applied methodology, mainly  
22 consisting of a double full preparation, first at larger grain size ( $\sim 0.4$  mm) and then at  $< 100$   
23  $\mu\text{m}$ , provides an appropriate procedure to separate suitable material to obtain the K-Ar age  
24 of the eruption, i.e. the sample's groundmass, in which there is no risk of the presence of  
25 older, inherited crystals. Our new geochronological data set gives an improved insight into  
26 the temporal construction of the Ciomadul volcanic complex, where (due to the method  
27 applied here) all ages are younger than those from previous studies that used whole-rock K-  
28 Ar ages. Our new results show that Ciomadul's volcanic activity began with the construction  
29 of the southeastern, peripheral domes from ca. 850 ka to 440 ka. After a ca. 250 ky long  
30 repose period, the activity resumed in the northern part at around 200 ka, with subsequent  
31 domes emplaced between 200 and 130 ka, aligned roughly north-south in the western-  
32 central part of the complex. Following a 30 ky long quiescence period, the eastern-central  
33 domes formed between 100 and 60 ka. In addition to the chronological history of lava dome  
34 volcanism, we also investigated the sequence of crystallisation of mineral phases present in  
35 the lavas with respect to the modification of eruption ages. Ages obtained on pure minerals  
36 (plagioclase, amphibole and biotite) are systematically older than those obtained on  
37 groundmass, showing that most of them formed up to 1.85 Myr before eruption in a long-  
38 lived, pre-Ciomadul magmatic system. Crystal size distributions (CSD) data support the age  
39 contrasts between juvenile groundmass and older inherited minerals. After injection of new  
40 magma and convective mixing with crystal clots, ascent of the resulting led to eruptions of  
41 material representing contrasting ages.

42 **Keywords**

43 K-Ar geochronology; groundmass; glomerocryst; excess argon; dacitic lava dome; crystal size  
44 distributions; Quaternary volcanism

## 45 **1 Introduction**

46 Accurate, high-temporal resolution data on eruption ages are crucial to better constrain  
47 the geochemical and petrological evolution of volcanic systems (e.g. Kersting and Arculus,  
48 1994; Hildenbrand, 2004; Cadoux et al., 2005), as well as to infer hazard parameters such as  
49 recurrence rates and repose periods (Marzocchi and Zaccarelli 2006; Damaschke et al. 2018;  
50 Reyes-Guzman et al. 2018). The more accurately the volcanic activity is known, the better its  
51 recurrence can be documented and its potential risk constrained (Turner et al. 2009). Such  
52 ages also allow estimates of magma extrusion rates (Crisp 1984; Singer et al. 1997) and  
53 detailed variations of eruption rates through time and space (Hora et al. 2007; Lahitte et al.  
54 2012; Germa et al. 2015). Moreover, eruption ages help identify vent migration patterns  
55 (Tanaka et al. 1986; Connor and Hill 1995; Condit and Connor 1996; Heizler et al. 1999) in  
56 dispersed, monogenetic volcanic fields (Nemeth and Kereszturi 2015), and volcanic  
57 processes, such as magma crystallisation, vesiculation and fragmentation, that are crucial for  
58 eruption forecasting in both monogenetic (Kereszturi et al. 2017) and polygenetic volcanic  
59 systems (Turner et al. 2011; Damaschke et al. 2018).

60 During its long-term evolution, the Miocene to Pleistocene volcanic activity of the Inner  
61 Carpathian volcanic chain in the Carpathian-Pannonian Region (CPR; Fig. 1) shifted south-  
62 eastward (Szabo et al. 1992; Lexa et al. 2010). This migration defined the Călimani-Gurghiu-  
63 Harghita (CGH; Kelemen – Görgényi - Hargita)<sup>1</sup> range, East Carpathians, Romania (Pécskay et

---

<sup>1</sup> Official Romanian names, when mentioned at first, are followed by locally used Hungarian names (in brackets), which is helpful for the reader in finding the names on local maps

64 al. 1995, 2006). The youngest centre of the CPR, Ciomadul (Csomád) volcano, is located at  
65 the south-easternmost tip of the CGH range. It is a dacitic lava domes complex truncated by  
66 the well-preserved twin craters of St. Ana (Szent Anna) and Mohoš (Szakács and Seghedi  
67 1995; Karátson et al. 2013). Ciomadul experienced a long-term eruptive history, producing a  
68 dozen lava domes emplaced during the last ca. 1 Myr over an area of 70 km<sup>2</sup> (Pécskay et al.,  
69 1995; Szakács et al., 2015). Its latest, mainly explosive, activity has been dated by  
70 radiocarbon and luminescence (OSL and post-IR IRSL) methods (Moriya et al. 1996; Vinkler  
71 et al. 2007; Harangi et al. 2010, 2015b; Karátson et al. 2013, 2016) around 32 ka. This has  
72 great significance for the regional, Late Quaternary tephrostratigraphy considering the areal  
73 distribution of these tephra which extend up to 350 km eastward (Karátson et al., 2016; Wulf  
74 et al., 2016). However, Ciomadul's whole volcanic history lacks a sufficiently constrained and  
75 reliable geochronological framework. Particularly, the recurrence time of the long-lasting  
76 dome-forming activity that preceded the explosive events is still poorly constrained.  
77 Previously obtained ages based on conventional K-Ar dating of the Ciomadul lava domes  
78 suffer from a lack of analytical accuracy (Pécskay et al. 1995; Szakács et al. 2015). An  
79 alternative approach, U-Th/He dating of zircon (Molnár et al. 2018), focused mostly on the  
80 onset of Ciomadul volcanism (around 1 Ma), without targeting the main area of the central  
81 dome complex.

82 Even Ciomadul have experienced a long dormant period to present , with no eruption in  
83 the past 10,000 years, it is susceptible to erupt again (Szakács et al. 2015). Indeed, magneto-  
84 telluric surveys suggest the presence of conductivity variations at various levels beneath  
85 Ciomadul that have been attributed to the presence of a partially molten magma body  
86 below the volcano (Harangi et al. 2015b). These authors interpreted these anomalies as a  
87 result of the presence of crystal-mush bodies containing about 5–15% melt fraction at

88 depths of 5-25 km and 30-40 km. These depths coincide with a low velocity seismic zone  
89 located by crustal tomography (Popa et al. 2012).

90 This paper aims to constrain the main history of extrusive activity of Ciomadul, focusing  
91 on the central dome complex and its peripheral lava domes. Due to the very young eruption  
92 ages (in the 100 ka range), apart from the  $^{40}\text{Ar}/^{39}\text{Ar}$  method, the unspiked Cassignol-Gillot  
93 technique (Cassignol and Gillot, 1982; Gillot et al., 2006), which uses the K-Ar radioactive  
94 chronometer, is arguably the most precise radiometric argon dating technique that can be  
95 applied to Ca-rich volcanic rocks. . The advantage of this technique is that avoids recoil issues  
96 of  $^{39}\text{Ar}$ ,  $^{37}\text{Ar}$ , and  $^{36}\text{Ar}$  in the reactor that may affect the  $^{40}\text{Ar}/^{39}\text{Ar}$  technique. The method has  
97 proven to be well-suited for dating recent up to Holocene lavas (Samper et al. 2009; Germa  
98 et al. 2011b; Gertisser et al. 2012). In part 1 of this work, we use this method to obtain  
99 precise eruption ages and constrain the geochemical evolution of the system. In part 2 we  
100 use the results to also assess the geomorphological evolution and magma output rates that  
101 characterized the evolution of Ciomadul's dome complex (Karátson et al., this volume). In  
102 this way we build on previous work using high-precision Cassignol-Gillot K-Ar geochronology  
103 at, for example, Basse-Terre (Samper et al. 2009), Martinique (Germa et al. 2011b, 2015) or  
104 Merapi (Gertisser et al. 2012), in illustrating how a detailed geochronological framework can  
105 support studies that also constrain magmatic evolution and time-space eruptive dynamism.

## 106 **2 Geological background**

107 As volcanic activity migrated south-eastward along the CGH range during the Miocene  
108 to Pleistocene (Pécskay et al., 1995, 2006), magma compositions evolved from normal calc-  
109 alkaline to high-K calc-alkaline and shoshonitic (Szakács et al. 1993). This evolution was in  
110 tandem with a decrease in magmatic output rates (Szakács and Seghedi 1995; Karátson and

111 Timár 2005). As decrease in the output rate is expressed by the progressive transition from  
112 large stratovolcanoes, occasionally with calderas, to smaller, mostly effusive cones and lava  
113 domes (Szakács and Seghedi, 1995; Karátson and Timár, 2005; Karátson et al., this volume).

114 Ciomadul volcano (Fig. 1) represents the best-preserved lava dome complex at the  
115 southernmost end of the CGH volcanic range. Its geological setting is presented in Szakács et  
116 al. (1993; 2015), Karátson et al. (2013; this volume), Harangi et al. (2015a) and Molnár et al.  
117 (2018). A dome complex is a special type of compound polygenetic volcano where an  
118 assemblage of nested lava domes, coulees (Blake 1990) and related pyroclastic and epiclastic  
119 volcanic rocks are spaced so closely in space and time that they are considered a polygenetic  
120 volcano rather than a group of monogenetic volcanoes (Lexa et al. 2010). Mostly high-K  
121 dacitic in composition, Ciomadul consists of domes resulting from extrusion of viscous  
122 magma and comprises the spatially and volumetrically most significant central dome in this  
123 system (Karátson et al., this volume). The system also includes the more isolated  
124 southeastern andesitic domes of Dealul Mare (Hegyes-tető) and the Puturosu (Büdös) Hills  
125 (Fig. 1), but these are not studied here. To the south, there are two other domes, which have  
126 andesitic to shoshonitic composition (Szakács et al., 2015). These latter domes, as well as the  
127 adjacent, western Pilișca (Piliske) stratovolcano in the South Harghita range are older than  
128 Ciomadul (Szakács et al., 2015; Molnár et al., 2018).

129 As already described elsewhere, such as at the Okataina Center in New Zealand's Taupo  
130 Volcanic Zone (Smith et al. 2004, 2005; Shane et al. 2007; Rubin et al. 2016), the magma  
131 batches of Ciomadul's dacites were probably produced as the result of reheating by  
132 intrusion(s) of hot mafic magma into a silicic reservoir (Kiss et al. 2014). In particular,  
133 crystallisation of amphibole has been related to the storage of a near-solidus silicic crystal  
134 mush body at 8 – 12 km depth (Kiss et al. 2014). The remobilization of silicic crystal mush can

135 provide a large amount of xenocrysts, which constitutes up to one third of the volume of the  
136 erupted silicic magma of some lava domes as observed, for instance, on Santorini or  
137 Montserrat (Zellmer et al. 2000, 2003). At Ciomadul, the role of these xenocrysts has yet to  
138 be shown and analysed. The xenocrysts, isolated or as part aggregates of crystals called  
139 glomerocrysts (or crystal clots), may have reached the surface with a part of the radiogenic  
140 argon ( $^{40}\text{Ar}^*$ ) they had accumulated since their formation, making K-Ar dating of the dacitic  
141 domes challenging. Indeed, these xenocrysts are carriers of extraneous argon, which are  
142 prone to bias K-Ar ages (Dalrymple and Moore 1968; Stipp et al. 1969; Ozawa et al. 2006).

### 143 **3 Petrology of the Ciomadul lava domes**

144 Detailed petrology of the Ciomadul lava domes was already well established by  
145 previous studies ((Kiss et al. 2014; Harangi et al. 2015b; Szakács et al. 2015)). We here only  
146 highlight their main characteristics. Ciomadul lava dome rocks are mainly high-K calc-  
147 alkaline, poorly vesicular dacites. Mainly porphyritic, these rocks contain 20-35 vol% coarse  
148 crystals (most of them being xenocrystic, see below) commonly set in a fine-grained, light-  
149 grey groundmass. In order of relative abundance, these include plagioclase ( $\text{An}_{85-30}$ , 10-25  
150 vol%), amphibole (5-13 vol%), biotite (1-4 vol%), orthopyroxene (1-2 vol%), and Fe-Ti oxides  
151 (1-2 vol%). Plagioclase occurs as euhedral laths up to 10 mm in size and often exhibits  
152 inclusions of green-brown biotite, euhedral amphibole, and sparse equant Fe-Ti oxide  
153 crystals. Euhedral crystals include mainly plagioclase, some exhibiting oscillatory zoning and  
154 sieve textures, and amphibole. Subhedral biotite is present as red-brown, pleochroic tabular  
155 laths up to 5 mm in length (Szakács et al. 2015). Red-brown hornblende (low-Al amphibole  
156 with thick breakdown rims) and pargasite (high-Al amphibole with thin reaction rims) are  
157 present as rounded, subhedral to anhedral crystals up to 10 mm in size (Kiss et al., 2014;

158 Harangi et al., 2015b), containing abundant inclusions of Fe-Ti oxides, plagioclase or biotite.  
159 From thermobarometrical modelling, formation of amphiboles has been interpreted as  
160 bimodal (Kiss et al., 2014); hornblende having formed at lower temperature (< 800°C) and  
161 pargasite having formed at higher temperature (950°C).

162 The dome rocks contain abundant glomerocrysts or crystal clots, which are aggregates  
163 of crystals. Importantly for dating, these glomerocrysts consist of remobilised crystals (> 1  
164 mm and up to 15 mm in diameter, Fig. 2) with microdiorite textures, containing mainly  
165 rounded and slightly altered plagioclase and amphibole, in addition to Fe-Ti oxides, apatite,  
166 biotite and zircon. Such remobilised crystals are here referred to as xenocrysts, whereas the  
167 term glomerocryst is used for an aggregate of xenocrysts remobilised from crystal mush. The  
168 groundmass of the dome lavas contains plagioclase, hornblende, biotite with occasional  
169 orthopyroxene, Fe-Ti oxide and glass.

## 170 **4 Methods**

### 171 4.1 Applying the unspiked Cassinot–Gillot K-Ar technique

172 The unspiked Cassinot-Gillot technique allows the accurate detection of low  
173 percentages of radiogenic  $^{40}\text{Ar}$  (Quidelleur et al., 2001). It has been applied to the dating of  
174 young (< 100 ka) volcanic events and successfully compared with other dating methods such  
175 as  $^{14}\text{C}$ ,  $^{36}\text{Cl}$  exposure and thermo-luminescence (Lahitte et al. 2001; Gillot et al. 2006; Germa  
176 et al. 2010; Schimmelpfennig et al. 2011). The technique was also favourably compared with  
177 the  $^{40}\text{Ar}/^{39}\text{Ar}$  method and gave similar results when applied to groundmass samples (Coulie  
178 et al. 2003; Calvert et al. 2006; Hildenbrand et al. 2014).

#### 179 4.1.1 *The unspiked Cassinot–Gillot technique*

180 Independent K and Ar measurements were performed in the Laboratoire GEOPS  
181 (GEOsciences Paris-Sud, Orsay, France). Following dissolution using a mixture of HF, nitric

182 and perchloric acids to destroy the silicate network, potassium (K) was measured by flame  
183 emission spectroscopy. Ar isotopic measurements were performed using a 180°-sector mass  
184 spectrometer (Cassignol and Gillot 1982; Gillot et al. 2006). This technique has a limit of  
185 detection for the radiogenic Ar content ( $^{40}\text{Ar}^*$ ) of only 0.1% of the total extracted argon  
186 (Quidelleur et al. 2001). Details of the Ar isotopic approach are given elsewhere (Cassignol  
187 and Gillot 1982; Gillot and Cornette 1986; Gillot et al. 2006) and are summarized in the  
188 Supplementary Material. To minimize the effect of mass-discrimination, the amount of  
189 radiogenic argon ( $\%^{40}\text{Ar}^*$ ) was calculated from a direct comparison between the  
190 instrumental  $^{40}\text{Ar}/^{36}\text{Ar}$  sample ratio and the instrumental  $^{40}\text{Ar}/^{36}\text{Ar}$  atmospheric ratio at  
191 identical pressure. Unlike the conventional K-Ar technique, this direct quantification does  
192 not add a  $^{38}\text{Ar}$  spike and is made possible by the very stable analytical conditions. Average  
193 relative uncertainties of the  $^{40}\text{Ar}/^{36}\text{Ar}$  ratios and on the amount of radiogenic argon ( $\%^{40}\text{Ar}^*$ )  
194 are 0.045% and 1.533%, respectively. The technique relies on the assumption that all the  
195 measured  $^{40}\text{Ar}^*$  comes from the in-situ radioactive decay of  $^{40}\text{K}$ .

#### 196 4.1.2 Sample preparation

197 Extraneous argon, i.e. argon not generated by *in situ* decay of potassium, originates  
198 from inherited argon and excess argon, and may bias K-Ar ages (Dalrymple and Moore 1968;  
199 Stipp et al. 1969; Ozawa et al. 2006). Inherited argon consists of the contamination by older  
200 minerals incorporated into the juvenile magma before eruption, whereas excess argon is  
201 introduced from outside the system, commonly from fluid circulations (Kelley, 2002). Our  
202 sample preparation procedure (from fieldwork sampling to the sample separation) aims at  
203 isolating the groundmass from such a source of extraneous argon. Given the incompatible  
204 nature of argon, mineral/fluid and mineral/melt partition coefficients range from 0.01 to as  
205 low as  $7 \times 10^{-6}$ , and excess argon remains a relatively uncommon phenomenon (Kelley, 2002).

206 On the other hand, extraneous argon may result from the contamination by older country  
207 rock (inherited argon in xenoliths), or by excess argon present either in inclusions of glass  
208 within phenocrysts (Dalrymple and Moore 1968) or in hydrous fluid in the grain boundary  
209 network (Kelley 2002). As K-Ar ages do not give spectra to check the presence of inherited  
210 argon, dates may be erroneously too old due to such contamination sources. However,  
211 accurate sampling, sample separation, and very strict selection of a narrow density range of  
212 pure groundmass greatly minimizes the risk of contamination due to the presence of  
213 extraneous argon.

#### 214 4.1.3 *Sample selection*

215 During two field campaigns (in October 2015 and June 2016), 25 samples (about 3 kg-  
216 weight each), were collected from Ciomadul's lava domes. The sample locations are shown  
217 in Figure 1 with the UTM coordinates listed in Table 2. Some of the sampled domes were  
218 assumed to be coeval with the late-stage (<50 ka) pyroclastic (fall and flow) deposits  
219 (Harangi et al., 2010, 2015a, Karátson et al., 2013, 2016; Wulf et al., 2016). In the field, only  
220 samples without visible obvious traces of alteration (calcite, zeolite, or any secondary  
221 minerals) and fluid circulation were collected. An additional inspection of thin sections, and  
222 checking the freshness of the groundmass, reduced the number of samples to be dated to  
223 18, representing nine individual lava domes. The low loss-on-ignition (LOI) values (less than  
224 1.6 wt%, Table 3) indicate that secondary weathering processes have not significantly  
225 affected the selected samples. These criteria reduce the possible bias of K-Ar ages related to  
226 K loss or gain via alteration.

#### 227 4.1.4 *Sample separation*

228 One of the main issues in determining the eruption age of the xenocryst-bearing  
229 lavas from the Ciomadul domes is to separate pure groundmass aliquots from numerous

230 xenocrysts and phenocrysts, which are potential carriers of extraneous argon. The  
231 probability of extraneous argon increases with the range of the groundmass density. Indeed  
232 aliquots having a large range of density may contain significant amounts of xenocryst and  
233 phenocryst fragments together with the groundmass. In our work, we lowered the relative  
234 density range to less than 0.05 (dimensionless quantity). To separate the groundmass as  
235 much as possible from inherited minerals, we applied a two-step procedure.

236         First, the whole-rock sample was crushed and sieved to the 250–500  $\mu\text{m}$  size fraction  
237 and then ultrasonically washed in 10% nitric acid solution in order to remove any traces of  
238 alteration (clay, sulphur, carbonate, etc.) and hydrothermal products (zeolites, salt  
239 containing chlorine compounds, some of them being that isobar to argon isotopes). Finally,  
240 the sample was rinsed with water, ethanol and acetone, and ca. 200 g clean material was  
241 obtained. Neither HF nor HCl acid were used during sample cleaning in order to avoid  
242 mass isobaric contamination (by HCl) that could bias the  $^{36}\text{Ar}$  detection or induce dissolving  
243 and loss of K (HF and HCl) as was observed in the study of Balogh et al. (2010). Groundmass  
244 aliquots were separated by means of heavy liquids (bromoform progressively diluted in  
245 ethanol) and, if necessary, by magnetic separation (Gillot et al. 1992). This procedure was  
246 efficient in separating the mixed grains of biotite/groundmass or amphibole/groundmass  
247 from the pure groundmass, although, in some cases, it was not possible to eliminate the  
248 mixed plagioclase/groundmass grains.

249         This first preparation step was followed by additional crushing to the 62.5-125  $\mu\text{m}$  size  
250 fraction (Fig. 3b). After cleaning, a second density separation was performed to isolate the  
251 groundmass fraction (Fig. 3c) from the remaining plagioclase crystals (Fig. 3d). Following the  
252 density separation, magnetic separation and handpicking were performed to guarantee the  
253 absence of plagioclases in the aliquots to be dated.

254 Pure phenocrysts and xenocrysts (K-feldspar, plagioclase, biotite and amphibole) were  
255 separated from the 250-500  $\mu\text{m}$  fraction in an attempt to estimate the contribution of  
256 inherited argon in whole-rock dating. We also separated plagioclase microphenocrysts from  
257 samples 16C1O01 and 16C1O04 as their groundmass was slightly altered.

#### 258 4.2 Crystal size distribution analysis

259 In order to highlight the petrographical properties of the Ciomadul dacitic lavas and, and  
260 determine its impact on the ideal fraction for K-Ar dating, crystal size distribution (CSD)  
261 analyses were obtained on representative samples, following standard methods (Higgins  
262 1996). High-resolution photomicrographs were taken and digitally merged together to  
263 create single large thin-section images. These images (6400  $\times$  4800 pixels) were imported  
264 into ImageJ software, where contrast and brightness were adjusted to highlight crystal  
265 boundaries. For each crystal population, including plagioclase (selected by white and/or  
266 bright zones) and mafic crystals (amphibole and biotite, orange to dark brown zones), colour  
267 histogram analyses and thresholding were applied to outline crystals. Small crystals (< 10  
268 pixels) were removed from these binary images. Best-fit ellipses were applied to determine  
269 long- and short-axis measurements. Mean crystal aspect ratios were calculated using the  
270 CSDSlice methodology (Morgan and Jerram 2006). For all grain categories, the number of  
271 measurements was at least 10 times higher than the minimum recommended (Mock and  
272 Jerram 2005; Morgan and Jerram 2006). Intersection lengths were converted to 3-D CSDs,  
273 using the CSDCorrections 1.6 software (Higgins 1996, 2002, 2006).  $L_{\text{max}}$  is calculated by  
274 averaging the four largest crystals within each identified population. The lower limit of the  
275 CSD was 0.010 mm (which is not necessarily the smallest crystal in the rock). Samples were  
276 classified as massive and approximate crystal roundnesses of 0.3 for plagioclase and 0.6 for

277 mafic crystals (on a scale of zero, angular, to one, spherical) were used. Logarithmic length  
278 intervals were used, with each bin  $10^{0.2}$  times the size of the previous bin. Bins with less than  
279 three crystals were removed from the CSD analysis. Where CSD slopes were curved or  
280 kinked, individual segments were interpreted using least squares regression.

#### 281 4.3 Petrographical and geochemical analyses

282 To highlight the importance of the main mineral phases, a petrographical analysis was  
283 performed in order to estimate the relative proportion of the main phenocrysts (plagioclase,  
284 biotite, and amphibole), xenocrysts, glomerocrysts and groundmass. Major-element whole-  
285 rock analyses were also performed on the newly dated lava rock samples by ICP-AES to  
286 assess the geochemical evolution through time. The samples were analysed at Bureau  
287 Veritas Minerals, Vancouver, Canada, following standard sample preparation and analytical  
288 techniques.

## 289 5 Results

### 290 5.1 Crystal size distribution analysis and justification of the groundmass separation process

291 Crystal size distribution data based on the major axis of the fitting ellipsoid and  
292 results are presented in Table 1. Almost all samples (black curves in Fig. 4a) show CSD plots  
293 for both plagioclase and mafic mineral phases that exhibit kinked profiles, allowing each to  
294 be divided into two individual segments. On the other hand, sample 16C1008 differs with its  
295 much more linear CSD profile (coloured curves in Fig. 4a), particularly for the mafic minerals.  
296 A downturn in the smallest crystal sizes can appear either from real population proportions  
297 or from analytical bias (Higgins 1996, 2002). Considered as representing a left-hand  
298 truncation effect, these bins were removed from analyses.

299 Plots for plagioclase show the most prominent kinked CSDs (black curve, Fig. 4b).  
300 Each curve can be divided into two distinctive segments, defined by sizes  $<0.125$  and  $> 1$   
301 mm. Volumetric plagioclase proportions range from 29.5 to 38.0 vol% and maximum length  
302 ( $L_{\max}$  in Table 1) from 2.93 to 4.79 mm. Average characteristic length values, defined as the  
303 opposite of the inverse of the slope (Marsh 1988), are around 0.02 mm for the smaller  
304 populations and range from 0.65 to 2.12 mm for the larger ones.

305 Mafic mineral (biotite) CSDs show concave-upward patterns that are smoother than  
306 those for plagioclase (grey curve, Fig. 4c) but kinked enough to divide trends into two slopes  
307 ( $<0.125$  and  $> 1$  mm). Volumetric mafic mineral proportions range from 7.9 to 12.3 vol% and  
308  $L_{\max}$  from 1.39 to 2.08 mm. Average characteristic length values range from 0.016 to 0.025  
309 mm for the smaller mafic populations and from 0.32 to 0.50 mm for the larger ones.

310 Using the method of Marsh (1988), and from the growth rates of plagioclase  
311 microphenocrysts estimated at around  $1 \times 10^{-10}$  mm s<sup>-1</sup> (Higgins and Roberge 2007),  
312 residence times for these populations are around six years. Such delay cannot be related to  
313 the magma ascent (estimated at 12 days by Kiss et al., 2014), but to the magma storage  
314 preceding eruption (Kiss et al., 2014; Harangi et al., 2015b).

315 CSD plots do not take into account more than 50 % of the total crystal volume (grey  
316 in Fig 4A insets). This is the population corresponding to grains smaller than 0.010 mm, and  
317 constitutes the microlitic groundmass. This population represents material that crystallised  
318 during the eruption.

319 As the microlitic fraction and microphenocrystic populations not contain pre-eruption  
320 inherited argon that may bias results, it represents the ideal fraction for eruption age  
321 determination. We hereafter refer to this population as groundmass. The 0.125 – 1 mm

322 fraction corresponds to the juvenile magma groundmass and the smaller phenocrysts,  
323 possibly inherited as xenocrysts. As a result, this population is not suitable for determining  
324 an eruption age. The > 1 mm fraction is mostly made up of pre-eruptive and, possibly,  
325 inherited-argon-rich minerals. As crushing would reduce the larger minerals into grains  
326 having the same size and almost the same density as the smaller minerals, simply crushing  
327 and separating them in a single-step procedure is not suitable. Groundmass aliquots were  
328 thus obtained during the two-step procedure described above (see also Fig. 3), with each  
329 separation step contributing to the maximum possible purification of the originally <0.125  
330 mm fraction by removing grains considered to have originated from phenocrysts or  
331 glomerocrysts, i.e. from any crystals initially larger than 0.125 mm.

## 332 5.2 K-Ar ages

333 K-Ar ages are reported in Table 2, with all uncertainties quoted at the one-sigma ( $1\sigma$ )  
334 level. Age calculations are based on the  $^{40}\text{K}$  abundance and decay constants  
335 recommended by Steiger and Jager (1977). The argon content is calculated from two  
336 independent measurements. As a higher abundance of radiogenic  $^{40}\text{Ar}^*$  means a lower  
337 uncertainty on the age, the average age and its  $1-\sigma$  uncertainty have been calculated by  
338 weighting each independent age measurement with its amount of radiogenic  $^{40}\text{Ar}^*$ .  
339 Percentages of  $^{40}\text{Ar}^*$  range from 1.03% to 34.3 vol%, with respective relative uncertainties  
340 between 6.48% and 0.27%. Relative errors of the ages are between 12.6% and 1.44%, the  
341 latter value being near the limit of our method set at 1.42% for a 100% radiogenic sample,  
342 i.e. when only the relative uncertainties on K-content (1%) and argon calibration (1%) affect  
343 the result. With the exception of sample 16C1O04, all Ar analyses were successfully  
344 duplicated at the  $1-\sigma$  level (Table 2). The poor reproducibility of sample 16C1O04 may reflect

345 grain heterogeneity within the sample. In this case, the uncertainty of the age was calculated  
346 as the standard deviation of the duplicated age measurements.

347 Even if our strict selection effectively removed phenocrysts, glomerocrysts and their  
348 fluid inclusions, greatly minimizing the risk of biasing ages by excess argon, we have to  
349 consider that the elimination of excess argon might not have been perfect. Such cases would  
350 induce eruption ages that are slightly younger than our results.

### 351 *5.2.1 South-eastern and northern domes*

352 Three new K-Ar ages constrain the emplacement time of the peripheral domes of the  
353 Ciomadul area (Table 2, Fig. 1 and Fig. 5) in addition to the somewhat older Dealul Mare. The  
354 radiogenic argon content ( $^{40}\text{Ar}^*$ ) of the dated samples varies from 4 to 35 vol%, this latter  
355 value being related to the exceptional freshness of the sample, yielding very low  
356 atmospheric contamination. The groundmass K content is homogenous, from 3.23 to 3.59  
357 wt%.

358 The two south-eastern peripheral domes of Muntele Puturosu (Büdös Hill) and  
359 Balványos (Bálványos Hill) represent relicts of apparently heavily eroded domes that cut  
360 through the Cretaceous flysch (Szakács et al., 1993, 2015). Muntele Puturosu was dated at  
361  $704 \pm 18$  ka (16C1O08). The Balványos dome, which is the south-easternmost volcanic  
362 extrusion of the Ciomadul area (Fig. 1), is dated at  $641 \pm 9$  ka (16C1O07) and  $440 \pm 12$  ka  
363 (16C1O06). Based on the more proximal position of 16C1O07 the 641 ka age may better  
364 constrain the emplacement age of the Balványos dome, and the younger sample could be  
365 linked to another, nearby eruption source no longer morphologically visible. Due to the small  
366 error even at the  $2\sigma$  level, it can be concluded that the two samples are from successive,  
367 adjacent eruptions separated by a long time gap.

368 In the north, the groundmass separated from the sample collected from the Haramul  
369 Mic (Kis-Haram) dome (16CIO01) shows very high atmospheric contamination. Therefore, no  
370 trustworthy age could be obtained on the groundmass. Instead, plagioclase  
371 microphenocrysts, which crystallized shortly before eruption were processed, giving an age  
372 of  $245 \pm 24$  ka. However, due to presence of glomerocrysts, the probability that the aliquots  
373 of plagioclase microphenocrysts contain inherited grains is not zero. As a consequence, the  
374 K-Ar age has to be considered a maximum value. Because Haramul Mic is the oldest part of  
375 the main dome complex, this age implies that most of the extrusive dome activity of  
376 Ciomadul was constrained within the past 250 ky.

#### 377 5.2.2 *Western-central part of the dome complex*

378 The most important results of our work are related to the western-central main part of  
379 the dome complex, which represents the largest volume of Ciomadul (Karátson et al., this  
380 volume). Of these domes, only Haramul Mare (Nagy-Haram), Dealul Cetății (Vár-tető), Dealul  
381 Taca (Fáca) and Piscul Pietros (Köves Ponk) have been dated by applying the conventional K-  
382 Ar technique (Pécskay et al. 1992, 1995; Szakács et al. 2015). In addition, Piscul Pietros was  
383 also dated by the U-Th/He method (Harangi et al. 2015a), whereas Dealul Cetății (Vár-tető)  
384 and Haramul Lerbos (Fű-Haram) were dated using uncorrected U-Th/He measurements  
385 (Karátson et al. 2013), only providing age ranges.

386 The obtained ages define a 50 ky time span from about 184 ka to 133 ka (Table 2, Fig. 1  
387 and Fig. 5), showing that the majority of the Ciomadul domes were formed in a relatively  
388 short time interval. The K-content varies from 1.39 wt% (on plagioclase microphenocrysts) to  
389 3.72 wt% (groundmass), whereas radiogenic argon contents ( $^{40}\text{Ar}^*$ ) range from 1.2 to 4.4  
390 vol%, inducing relative uncertainties between 3 and 14%. The Dealul Cetății (Vár-tető) dome  
391 in the north has been dated at  $184 \pm 5$  ka (sample 15CIO01), whereas the Vârful Comlos

392 (Kömlös-tető) dome (sample 16C1002) yielded an age of  $144 \pm 4$  ka. Adjacent to Vârful  
393 Comlos, the dome of Ciomadul Mare (sample 16C1004) represents the northern rim of the  
394 twin-craters of St. Ana and Mohoş, and may morphologically correspond to an older, larger  
395 explosion crater (Karátson et al. 2013; Szakács et al. 2015) created during the early Mohoş  
396 explosive eruptions. To minimize risk of contamination by gas released during the last  
397 explosive phase from the younger craters, and because the St. Ana crater area is still  
398 experiencing gas emanation, the material retained to date this dome consisted of plagioclase  
399 microphenocrysts. These were separated by the two-step procedure from the 40 – 80 µm  
400 grain size fraction obtained after crushing the 80 - 160 µm groundmass fraction. The very  
401 small grain size used in both steps allowed minimization of the traces of inherited minerals.  
402 The extracted plagioclase microlite fraction, which is expected to be contemporaneous with  
403 the eruption, provided an age of  $133 \pm 18$  ka (Table 2), indistinguishable from the Vârful  
404 Comlos data, even at  $1\sigma$  level.

#### 405 5.2.3 Eastern-central part of the dome complex

406 After a quiescence lasting tens of thousands of years, volcanic activity resumed at  
407 around 100 ka to form the eastern-central domes (Fig. 1). The Haramul Mare dome (sample  
408 15C1009), has been dated at  $96 \pm 2$  ka (Table 2). At the southern rim of the Mohoş crater, a  
409 rock sampled on the active face of a quarry offered access to a fresh sample of the Piscul  
410 Pietros (Köves Ponk) dome, which is morphologically truncated by the Mohoş crater. It has  
411 been dated at  $60 \pm 5$  ka (sample 16C1009, Table 2).

### 412 5.3 Geochemistry of the lava domes

413 Representative chemical analyses of the dated samples are given in Table 3.  
414 Concentrations of SiO<sub>2</sub> for the Ciomadul lava domes range between 62.8 and 68.4 wt%, and  
415 belong to the high-K calc-alkaline (HKCA) series. There is a dacitic composition for all but two

416 samples of the Balványos dome (16CIO06 and 16CIO07), the latter straddling the boundary  
417 with the high-K andesite field (Fig. 6a). We note that the southern Dealul Mare dome, not  
418 studied here, also falls in this latter andesite field (Szakács et al., 2015).

419 Major element contents (using SiO<sub>2</sub> as a differentiation index; Fig. 6b) show that MgO,  
420 CaO, Al<sub>2</sub>O<sub>3</sub>, MnO, Fe<sub>2</sub>O<sub>3</sub>, P<sub>2</sub>O<sub>5</sub> and TiO<sub>2</sub> decrease with SiO<sub>2</sub>, whereas K<sub>2</sub>O slightly increases; as  
421 does Na<sub>2</sub>O but with a more scattered distribution. These evolutionary trends are consistent  
422 with fractional crystallization of plagioclase, amphibole, pyroxene, biotite and Ti-Fe oxides.  
423 Specifically, the decreasing trends of CaO and Al<sub>2</sub>O<sub>3</sub> as SiO<sub>2</sub> increases, for all samples but  
424 16CIO08, are explained by predominantly plagioclase fractionation.

## 425 **6 Discussion**

### 426 6.1 Timing of lava dome activity

427 Our new K-Ar ages for the extrusive products of the Ciomadul lava dome complex  
428 allow better constraints on its dynamism. In particular, they reduce the age range previously  
429 suggested by Pécskay et al. (1995) and Szakács et al. (2015), showing that the mainly  
430 extrusive, dome-building activity occurred in two main stages and is younger than 1 Ma.

431 Our derived ages indicate that two stages can be distinguished in the construction of  
432 the Ciomadul system. The first stage (Table 2) produced the south-eastern peripheral domes  
433 of Muntele Puturosu and Balványos (Figure 1). In addition to the somewhat older Dealul  
434 Mare (Szakács et al. 2015; Molnár et al. 2018), the duration of this stage is constrained  
435 between around 850 and 440 ka. The second, and volumetrically most significant, stage of  
436 Ciomadul, began around 200 ka with the Haramul Mic dome-forming eruption. This stage  
437 built the northern and central portions of the dome complex. In turn, the main lava domes  
438 that form this second stage can be divided into two phases, an older phase between 200 and

439 130 ka and a younger phase beginning around 100 ka. Within the second phase, the 60 ka  
440 age of Piscul Pietros roughly coincides with the onset of the late-stage explosive eruptions  
441 (Harangi et al. 2015a; Karátson et al. 2016). Overall, the activity of the Ciomadul lava-dome  
442 complex is aligned approximately north-south, sub-parallel to a local fault (Matenco et al.  
443 2007). This suggests a tectonic control on magma extrusion which was characterized by two  
444 stages, separated by a long repose of ca. 440-200 ka. Dome eruptions over the main eruptive  
445 stage of Ciomadul (< 200 ka) point to a recurrence time of ca. 30 ka. Such an interval is in the  
446 same order of magnitude as the age of the latest volcanic event (Karátson et al., 2016),  
447 confirming the dormant (i.e. not extinct) status of the volcano as also suggested by fumarole  
448 activity (Vaselli et al. 2002; Kis et al. 2017), seismic tomography (Popa et al. 2012), and  
449 magnetotelluric surveys (Kiss et al. 2014; Harangi et al. 2015b).

## 450 6.2 Comparison with previous radiometric results

451 The issue of obtaining radiometric ages from whole-rock has been demonstrated  
452 elsewhere as possibly inducing biased results (Hofmann et al. 2000; Samper et al. 2007;  
453 Germa et al. 2011a). For instance,  $^{40}\text{Ar}/^{39}\text{Ar}$  dating of lava domes on Montserrat yielded an  
454 age of  $223 \pm 7$  ka using whole rock, whereas groundmass measurements produced an age of  
455  $155 \pm 5$  ka (Harford et al. 2002). The same study on the active dome obtained a surprisingly  
456 old age of  $426 \pm 95$  ka on pure plagioclase and only  $21 \pm 22$  ka on the groundmass fraction.  
457 This bias is particularly significant for young samples where any contamination effect would  
458 be magnified proportionally to the small amount of in-grown radiogenic Ar. In contrast to  
459 various crystal phases, the groundmass is the last phase to crystallize when the lava cools  
460 upon eruption. It is thus enriched in incompatible elements, including potassium, and in

461 elements which are in equilibrium with the atmosphere. Hence the initial argon isotopic  
462 ratios in the groundmass are atmospheric, and are devoid of radiogenic argon ( $^{40}\text{Ar}^*$ ).

463 Szakács et al. (2015) excluded the possibility of overestimated ages as they considered  
464 quartz phenocrysts as the most likely source of excess argon, which are very uncommon in  
465 the Ciomadul lavas (Kiss et al., 2014). However, as seen in Table 4 and Fig. 4, our groundmass  
466 ages contrast with those obtained from whole rock analyses by applying the conventional K-  
467 Ar method (Pécskay et al. 1995; Szakács et al. 2015). Only one sample (16C1O08, M. Puturosu  
468 dome) has an age ( $704 \pm 18$  ka); compatible at 1- $\sigma$  level with that obtained from whole rock  
469 by the conventional K-Ar technique ( $710 \pm 40$  ka, Table 4). For the remaining samples,  
470 considering the 2- $\sigma$  level, only two out of the seven ages match, but these agreements are  
471 mostly due to the large uncertainties on conventional K-Ar results (Fig. 5; Table 4).

472 Biotite from the Piscul Pietros dome, which was dated by both techniques, gave  
473 comparable ages of  $290 \pm 110$  ka by conventional K-Ar (Szakács et al. 2015) and  $196 \pm 4$  ka by  
474 the unspiked Cassinol-Gillot technique (this work); again the overlap of the ranges is only  
475 due to the very large error of the former. On the other hand, neither of these two ages are  
476 consistent with the age of  $560 \pm 110$  ka initially proposed by Pécskay et al. (1992).

477 Our groundmass dating of the Balványos dome, the south-easternmost Ciomadul  
478 dome (Fig. 1), yielded ages of  $641 \pm 9$  ka (16C1O07) and  $440 \pm 12$  ka (16C1O06), in contrast to  
479 previous ages of  $920 \pm 180$  ka and  $1020 \pm 150$  ka obtained by whole-rock K-Ar dating  
480 (Pécskay et al. 1995). Again, the minimal overlap (at  $2\sigma$ ) with the age obtained by the  
481 unspiked Cassinol-Gillot technique is only due to the very large error. Consequently, it is  
482 likely that these ages would not be coeval, if measured with the same range of uncertainties.  
483 It thus involves a possible shift toward older ages for the whole-rock K-Ar measurements,  
484 mostly induced by inherited argon.

485 One of the most controversial ages of Ciomadul was assigned to the northernmost  
486 dome, Haramul Mic (Kis-Haram), with an unpublished K-Ar age of 0.85 Ma (without reported  
487 uncertainties by Casta (1980), quoted in Szakács et al. 2015). Karátson et al. (2013) argued  
488 that the recent “pancake” shape of the dome (which is in contrast to other, high and steep-  
489 sided Peléan domes and coulées of Ciomadul) is not due to the old age, but simply reflects  
490 the original flat dome shape. Indeed, we dated this dome at  $245 \pm 24$  ka using plagioclase  
491 microphenocrysts, which provides a maximum age. Szakács et al. (2015) also reported a K-Ar  
492 age of  $210 \pm 50$  ka obtained from a block 2 km west of the dome. In agreement with this  
493 date, our dating confirms that, after at least a ca. 250 ky-long quiescence, extrusive activity  
494 resumed at Haramul Mic less than 250 ka ago.

495 The systematic offset between groundmass and whole rock ages can be related to an  
496 extraneous  $^{40}\text{Ar}$  component in the whole rock measurement, which comes from the  
497 inclusion of xenocrystic minerals. To evaluate the effect of extraneous  $^{40}\text{Ar}$  on age results,  
498 we conducted a component analysis on a thin section of sample 15CIO01 (Fig. 3a), whose  
499 groundmass was dated at  $184 \pm 5$  ka. Our aim was to calculate a whole-rock age by  
500 combining ages of the groundmass and the plagioclase fraction (the two dominant phases)  
501 with respect to their proportions in the sample. For the calculation, the thin section image  
502 was converted to a black and white image by setting a threshold. Below a value of 20% on  
503 the gray scale pixel is converted in black, otherwise is converted in white. This allows us to  
504 distinguish plagioclase (in white in Fig. 7a) from groundmass (in black). Because of the  
505 sample grain size (200  $\mu\text{m}$ ), the composition was next simulated by averaging the tone of  
506 each 200  $\mu\text{m}$ -wide subset (i.e. 40 pixel-wide square zones on the image). The composition  
507 was then defined on the grey scale, from a material of pure plagioclase (100% on grey scale,  
508 i.e. white on Fig. 7a), to one fully composed of groundmass (0% on grey scale, i.e. black on

509 Fig. 7a), including mixed material defined by an intermediate tone on grey scale (Fig. 7a). In  
510 order to highlight the composition of each grain, a colour map is also proposed (Fig. 7b).  
511 Pure plagioclase and pure groundmass grains are coloured in yellow and blue, respectively.  
512 Mixed grains are illustrated by variation of red lightness: black for grain having a composition  
513 almost similar of a groundmass grain, red for the perfectly intermediate composition (50%  
514 groundmass - 50% plagioclase), white for grain having a composition almost similar of a  
515 plagioclase grain (Fig. 7b). The age of each grain population was then modelled by  
516 considering its plagioclase/groundmass ratio (dotted black curve in Fig. 7c). The thin section  
517 reveals a composition of about 11 vol% of pure plagioclase dated at 1.1 Ma (Table 5), 60  
518 vol% of pure groundmass dated at 184 ka (Table 1), and 29 vol% of mixed grains with mixed  
519 ages (Fig. 7c). Applying the mixing theory to our multiphase and multi-age sample (Boven et  
520 al. 2001), the whole rock age can be constrained by weighting each grain population age by  
521 its proportion of the total:

$$522 \quad A = (\sum a_i \times p_i \times K_i) / (\sum p_i \times K_i) \quad (\text{Eq. 1})$$

523 where  $a_i$ ,  $p_i$  and  $K_i$  are ages (right Y-axis values in Fig. 7c), proportions, and K-contents of  
524 each grain population  $i$ , respectively. Such a calculation using a whole rock age model gives  
525  $320 \pm 8$  ka, 74% older than the groundmass age of  $184 \pm 5$  ka, and in agreement with the  $400$   
526  $\pm 160$  ka age previously obtained from whole rock data for the same dome (Szakács et al.  
527 2015). The whole rock model age shows the effect of only superficially removing the  
528 inherited xenocrysts from groundmass, as performed in the previous K-Ar studies.

529 A relationship between the volume percentages of glomerocrysts and inherited  
530 radiogenic argon was also assessed (Table 4). To apply this, the volume percentage of  
531 glomerocrysts is obtained from thin section analysis, and a proxy of inherited radiogenic  
532 argon is calculated as follows:

533 
$${}^{wr}Ar_i = ({}^{wr}Age - {}^{gm}Age) / {}^{wr}A \quad (Eq. 2)$$

534 where  ${}^{wr}Ar_i$  is the percentage of radiogenic argon assumed to have originated from inherited  
535 minerals, and  ${}^{wr}Age$  and  ${}^{gm}Age$  are the ages obtained from whole rock and groundmass  
536 analyses, respectively. All samples dated by both techniques were considered. The sample  
537 with no glomerocrysts (16CIO08, M. Puturosu dome) is the only one that does not display  
538 inherited argon as the whole rock and groundmass ages are coeval. It is also the sample  
539 where the CSD plot presents the most linear relationship. This can be taken as a sign of a  
540 single crystal population, or a minimal proportion of inherited crystals (coloured curves in  
541 Fig. 4a). On the other hand, sample 15CIO09 (Haramul Mare dome) has a 25 % glomerocrysts  
542 content by volume, and  $84 \pm 35$  % of its radiogenic argon originates from inherited argon  
543 (Table 4). A good correlation (Pearson correlation coefficient  $R \sim 0.95$ ) exists between  
544 glomerocryst abundance and inherited radiogenic argon (Fig. 7). This correlation remains  
545 good even if the glomerocryst-free sample (of M. Puturosu) is omitted. The correlation  
546 between glomerocryst abundance and inherited radiogenic argon allows a corrected age for  
547 the Dealul Tața dome to be derived. Thin section analysis of the same dome lava, as dated  
548 on whole rock at  $430 \pm 50$  ka by Szakács et al. (2015), displays a 23 vol% glomerocryst  
549 content. It contains  $85 \pm 20$  % of inherited argon (blue thin lines in Fig. 8) which implies an  
550 age of  $64 \pm 61$  ka. This age is still poorly constrained but is consistent with those obtained  
551 here for the same area across which are younger than 144 ka (Fig. 1).

552 Some of our new K-Ar ages are in good agreement with published (U–Th)/He ages  
553 (Karátson et al. 2013; Harangi et al. 2015a; Molnár et al. 2018). For the M. Puturosu dome,  
554 the (U–Th)/He age of  $642 \pm 44$  ka (Molnár et al. 2018) is similar to both the conventional K-Ar  
555 age of  $710 \pm 40$  ka (Szakács et al. 2015) and our new K-Ar age of  $704 \pm 18$  ka, which are all  
556 coeval at  $2\sigma$ . Also, our new ages for the Balványos dome,  $641 \pm 9$  ka and  $440 \pm 12$  ka, are

557 similar to the  $583 \pm 30$  ka (U-Th)/He age of Molnár et al. (2018). Note, however, that there is  
558 a strong alteration of the dome rocks of the Balványos summit, close to where the (U-Th)/He  
559 age was obtained (Molnár et al. 2018). Instead, both our dated samples were taken at the  
560 periphery of the dome from talus debris containing fresh rocks. Of these samples, the  
561 position of 16C1007 is the most proximal to the dome, and therefore the  $641 \pm 9$  ka date is  
562 that proposed to constrain the Balványos dome extrusion; overlapping with the  $583 \pm 30$  ka  
563 (U-Th)/He age at  $2\sigma$ .

564 The Haramul Mic dome was dated at  $163 \pm 11$  ka by (U-Th)/He by Molnár et al. (2018).  
565 This is only slightly different (at  $2\sigma$ ) from our age obtained from plagioclase  
566 microphenocrysts ( $245 \pm 24$  ka). In this case, because our age was considered as a maximum,  
567 the younger (U-Th)/He age is more likely. The similar age obtained by both methods  
568 confirms the conclusion that the main lava dome activity of Ciomadul started at around 200  
569 ka.

570 On the other hand, there are also a number of (U-Th)/He ages which are not in  
571 agreement with our dates. Of these, the results proposed for the Dealul Cetății dome are not  
572 coeval even at  $2\sigma$ :  $184 \pm 5$  ka (this study) and ca. 116 – 142 ka (Karátson et al., 2013). Also,  
573 the Piscul Pietros (Köves Ponk) dacitic dome yielded an age of  $60 \pm 5$  ka (this study), which is  
574 older than the (U-Th)/He age obtained from zircon ( $42.9 + 1.4 - 1.5$  ka) by Harangi et al.  
575 (2015b). In this latter case, that the (U-Th)/He age is possibly too young could be due to  
576 three reasons. First, the (U-Th)/He age is significantly lower than the 380 ka-long U-Th  
577 secular equilibrium (Farley et al. 2002), consequently it correction of the U-Th concentration  
578 at the scale of each dated zircon (Schmitt et al. 2010; Danisik et al. 2012), making the ages  
579 very sensitive to the accuracy of such a correction. Secondly, for the Piscul Pietros dome,

580 only four zircons were dated, and only the three oldest are coeval, thus the youngest age  
581 should not be considered when calculating the average age. Using only the 3 coeval zircon  
582 ages yields an age of about  $46 \pm 4$  ka which is closer to, and compatible with, our K-Ar age at  
583  $2\sigma$ . Thirdly, extraneous argon from an incomplete removal of xenocrysts for the  
584 overestimation of the K-Ar age, as well as partial loss of helium for the underestimation of  
585 the (U–Th)/He age, cannot be totally excluded. However, extraneous Ar effects, based on  
586 the careful sample preparation are considered minor, if not negligible.

### 587 6.3 Difference between groundmass and xenocryst mineral ages

588 To demonstrate the occurrence of inherited argon, a whole-rock age determination  
589 was carried out for the Haramul Mare dome (sample 15CI009, Table 4) following our unspiked  
590 K-Ar technique. Several K-bearing phases were also dated to identify which of them were the  
591 most susceptible to bias by inherited argon (Table 5 and Fig. 8). With the exception of  
592 plagioclase from M. Puturosu dome, all ages were significantly older than the groundmass  
593 ages (Tables 2 and 5). Consequently, the younger the juvenile lava of the dome is, the more  
594 important the influence of the xenocrysts is on the biased whole-rock age.

595 The effect of single-step or two-step separation has been assessed by processing two  
596 aliquots of sample 15C1001. The groundmass obtained from single-step separation gave an  
597 age of  $202 \pm 6$  ka, whereas an age of  $184 \pm 5$  ka (i.e. 10% younger) was obtained from the  
598 two-step separation (Fig. 10). This age difference can be related to inherited argon from the  
599 plagioclase fraction remaining after the single-step separation, assuming that the crystals  
600 originate from grains larger than 0.125 mm, i.e. from the size range on the CSD plot that  
601 corresponds to the mixing between grains from both grain-size populations (Fig. 4b). As the  
602 plagioclases from the glomerocrysts are significantly older ( $\sim 1.4$  Ma, see below) than the

603 eruption age ( $184 \pm 5$  ka), even a tiny remnant of them within the dated groundmass will  
604 produce an overestimated age.

605 The same issue of inherited glomerocrysts can also be encountered for the late-stage  
606 pyroclastic deposits that drape the lower flanks of the Ciomadul dome complex (Karátson et  
607 al., 2016). The BIX-2 block-and-ash flow deposit,  $\sim 3$  km south of Lake St. Ana and  $\sim 1$  km east  
608 of Bixad village (Fig. 1), for instance, is considered younger than 50 ka (Vinkler et al., 2007;  
609 Harangi et al., 2010; Karátson et al., 2016), whereas biotite phenocrysts contained within the  
610 sample of lava-dome rock yielded an age of  $561 \pm 19$  ka (15C10X2), categorizing them as  
611 xenocrysts. We note that this age is coeval with the age obtained from biotite xenocrysts  
612 ( $569 \pm 9$  ka, Table 5) from the Dealul Cetății dome ( $184 \pm 4$  ka, Table 1 and Fig. 1) located 4  
613 km to the north, suggesting that for both eruptions (BIX-2 block-and-ash flow and Dealul  
614 Cetății dome) the xenocrysts were inherited material originating from the same crystal  
615 mush.

616 The most extreme shift is encountered for the plagioclase glomerocrysts of the Vârful  
617 Comlos dome (16C1002, Table 5). These were dated at  $1848 \pm 27$  ka, compared to  $144 \pm 4$  ka  
618 from the groundmass. Considering the freshness of the sample, the loss of potassium (which  
619 would increase the age) can be ruled out and, consequently, these plagioclases are  
620 considered as the oldest inherited phase incorporated in any rock sample of Ciomadul.  
621 Notably, their old age is in the range obtained for the adjacent Pilișca volcano (Pécskay et al.,  
622 1995; Szakács et al., 2015; Molnár et al., 2018; Karátson et al., this volume).

623 The presence of inherited glomerocrysts indicates that the dated lava dome samples  
624 do not have a single crystallization age. Furthermore, these lavas contain minerals having  
625 experienced a multi-stage crystallization history, as also confirmed by the abundance of

626 oscillatory zoning in the larger plagioclase population (see, for instance, those in Fig. 3a).  
627 Similar assimilation of inherited argon in plagioclase, hornblende and biotite has been  
628 reported for the Youngest Toba Tuff eruption ( $74 \pm 4$  ka), where these minerals show K-Ar  
629 ages predating the eruption by as much as 1.5 Ma (Gardner et al. 2002). In the context of  
630 Ciomadul, it has previously been suggested that the crystal mush residing beneath the  
631 volcano was rapidly (in  $< 100$  y) remobilized by mafic magmas prior to the latest eruptions  
632 after tens of thousands of years of quiescence (Harangi et al. 2015a), as also observed in  
633 New Zealand at Taupo (Cole et al. 2014).

634         The following two arguments suggest that the older ages are due to the presence of  
635 argon inherited from the most retentive mineral phases: (1) the rather good correlation  
636 between K-Ar ages from the groundmass and the (U-Th)/He ages, and (2) the contrast  
637 between groundmass ages and pure mineral phase ages. This latter contrast would not be so  
638 important in case of a generalized contamination of the magma by excess argon. Indeed,  
639 excess argon tends to be relatively uncommon in minerals from silicic volcanic rocks largely  
640 because argon is highly incompatible in all major igneous minerals (Kelley 2002). As already  
641 described for Ciomadul (Kiss et al. 2014) and elsewhere (Singer et al. 1998; Stewart 2010;  
642 Doherty et al. 2012), the presence of glomerocrysts suggests a long-residence storage of  
643 silicic crystal mush in an upper crustal storage zone about 8-12 km below the surface. This  
644 may have been remobilized by any subsequent eruption of the dacitic magma (Kiss et al.  
645 2014). At Ciomadul, our geochronological data show that a significant proportion of the  
646 'phenocrysts' in the porphyritic dacites of Ciomadul are in fact old glomerocrysts.

647         Magma mixing is a widespread igneous phenomenon of variable importance,  
648 particularly evident in systems where a vapor-saturated magma reservoir occurs (Anderson  
649 1976). Such mixing between highly crystallized remnant magma of preceding activity with

650 newly injected hot magma prior to eruption has been observed in other volcanic settings  
651 such as Unzen (Nakamura 1995), the Mascota - Amatlán de Cañas volcanic fields (Luhr et al.  
652 1989; Gomez-Tuena et al. 2011) and the Palma Sola volcanic field (Gomez-Tuena et al. 2003)  
653 in the Trans-Mexican Volcanic Belt volcanism. Of these cases, the Los Azufres volcanic field  
654 (Mexico) shows evidence of the presence of a quartzo-feldspathic crystal-mush, located at a  
655 depth of around 5 – 10 km (Rangel et al. 2018). Large sanidine, quartz, plagioclase, and  
656 amphibole phenocrysts and mineral clots were assimilated from this mush by a melt  
657 extraction process, probably triggered by the arrival of a hotter magma at the base of the  
658 crystal-mush. This juvenile magma in turn caused reheating and partial melting of the  
659 quartzo-feldspathic crystal-mush (Rangel et al. 2018).

660 The size effect of the analysed minerals has also been checked by dating of  
661 plagioclases from samples 16CIO02, 16CIO04 and 16CIO09 (250-500  $\mu\text{m}$  fraction from single-  
662 step preparation and 63-125  $\mu\text{m}$  fraction from two-step separation). In all cases (Table 5 and  
663 Fig. 8), the larger-sized fraction size gave the oldest ages. This systematic shift toward older  
664 ages of large grains substantiates that the population of large plagioclase crystals contains  
665 inherited glomerocrysts. The case of sample 16CIO09 is extreme, as the small plagioclase  
666 grains gave an age of  $201 \pm 5$  ka, three times older than the groundmass age ( $60 \pm 5$  ka) but  
667 also five times younger than that obtained on large plagioclase xenocrysts ( $981 \pm 15$  ka). This  
668 finding implies that in the two-step fraction a significant amount of inherited plagioclase  
669 remained in addition to juvenile minerals that crystallised during lava dome cooling. These  
670 inherited minerals are either anhedral glomerocrysts (Fig. 3a), or euhedral and zoned  
671 individual phenocrysts of plagioclase (Fig. 3a) that must have formed in the magma storage  
672 system prior to eruption. Unfortunately, because of the contrast between eruption and  
673 inherited mineral ages (which has a difference by a factor of up to 16 in sample 16CIO09),

674 even a small portion of inherited plagioclase remaining in the microphenocrystic fraction  
675 extracted from the two-step separation will significantly increase the age obtained. This is  
676 the reason why we suggest considering the ages obtained on plagioclase microphenocrysts  
677 as maximum ages (16C1001 on Haramul Mic and 16C1004 on Ciomadul Mare domes). A  
678 similar age range (1 Ma) between multiple dated fractions has been observed on a single  
679 basaltic lava sample (from the Tihany Maar Volcanic Complex, Western Hungary) from eight  
680 groundmass aliquots showing various density and magnetic properties (Balogh and Nemeth  
681 2005). In this later case, due to a much older eruption age ( $7.92 \pm 0.22$  Ma), the difference  
682 between the different dated fractions shows less contrast (only 20% of excess). However, as  
683 in our study, the oldest age comes from aliquots showing the highest contamination by  
684 inherited minerals, while the groundmass aliquot, whose age is closest to that of the  
685 eruption, i.e. almost free of inherited minerals, is light and magnetic.

#### 686 6.4 Magmatic origin of inherited minerals

687 The apparent presence of inherited argon in the minerals of Ciomadul leads to  
688 questions regarding their origin with respect to the argon diffusion law in silicate minerals.  
689 Closure temperatures calculated for volume diffusion (e.g. Dodson, 1973) predict that at  
690 supra-solidus temperatures, and with extended residence time ( $> 1$  ky), every major mineral  
691 phase in these magmas should have remained fully open to argon loss prior to eruption. To  
692 explain the presence of inherited argon in magmas, it has been suggested that the  
693 incompletely reset minerals were xenocrysts with short ( $\sim 10$  years) residence times  
694 (Gansecki et al., 1996; Singer et al., 1998; Gardner et al., 2002). This mechanism is  
695 particularly likely for relatively small ( $< 10$  km<sup>3</sup>) magma bodies (Singer et al. 1998), such as  
696 those of Ciomadul. Similar processes operating over similar time scales has been observed at

697 different volcanic context, for instance : (1) the Taupo Volcanic Zone, New Zealand, where a  
698 large variations in crystallinity and long magma time residence (up to 250 ky, i.e. same order  
699 of magnitude as in Ciomadul) are shown (e.g. Brown et al., 1998; Brown and Fletcher, 1999;  
700 Matthews et al., 2012); (2) ongoing eruption of Unzen (Japan) where dacite is formed by  
701 mixing of relatively high- and low-temperature end-member magmas (Nakamura 1995;  
702 Nishimura et al. 2005). Thermo-mechanical considerations suggest that an effective  
703 reactivation of crystal mush is possible when the melt content in the magma reservoir  
704 increases to ~60%, allowing eruptible magma to coalesce (Bachmann and Bergantz 2004;  
705 Huber et al. 2011).

706 At Ciomadul, the source of glomerocrysts may be from previous crystallised magma of  
707 Ciomadul, i.e. from a disrupted crystal mush (Kiss et al., 2014). The thermobarometrical  
708 analysis of amphibole (hornblende and pargasite) crystallisation present in Ciomadul rocks  
709 shows that hornblende is xenocrystic, despite the importance of this phase in some domes  
710 (Kiss et al. 2014). Plagioclase is present both as inherited glomerocrysts and phenocrysts,  
711 because it displays ages either older than (samples 15CIO01, 16CIO02, 16CIO09) or similar  
712 (16CIO08) to the groundmass ages. Crystal clots of hornblende and plagioclase observed in  
713 some domes (samples 15CIO01, 16CIO02, 16CIO03, 16CIO04, and 16CIO09) suggest that the  
714 glomerocrystic material came from sources up to 1.85 Ma old (the oldest age obtained at  
715 Ciomadul). Such populations of older crystals contain variably argon-inherited content,  
716 explaining spuriously old ages that are common in differentiated lava domes in an arc  
717 context (Harford et al. 2002; Zimmerer et al. 2016).

718 The dominant mechanism for the generation of kinked CSD profiles is magma mixing.  
719 This preserves a steep slope for small-sized grains and adds a gentler slope for larger sized  
720 crystals, regardless of their proportions (Higgins, 2006). The larger population

721 (phenocrysts/glomerocrysts) can be identified as crystals inherited from one of the parental  
722 magmas (crystal mush), whereas the finer population (microphenocrysts) originated from  
723 the juvenile parent magma, in addition to the microlitic groundmass. Profiles of CSD data  
724 that are particularly kinked validate such a scenario. The fact that both mafic mineral phases  
725 and plagioclase show exceedingly similar kinked CSD spectra (i.e. an abnormally large  
726 amount of coarse grains) in the Ciomadul lavas strongly supports deep-seated storage as a  
727 common feature of this magmatic contribution (Armienti et al. 1994).

728         The oldest reliable eruption age of the dacitic domes of Ciomadul is around 700 ka  
729 (Muntele Puturosu dacitic dome). Another Ciomadul-type dacite dome adjacent to the  
730 Pilișca volcano, Bába Laposa ( $942 \pm 65$  ka), and the andesitic dome of Dealul Mare ( $842 \pm 53$   
731 ka), both dated by (U-Th)/He method (Molnár et al., 2018), are just slightly older. Therefore,  
732 the old age obtained on the inherited plagioclase phase (1.85 Ma) points to assimilation of  
733 xenocrysts from earlier magmatism, possibly that of the Pilișca volcano itself (Fig. 1).  
734 Incorporation of quite old xenocrysts from a crystal mush into dacitic magmas similar to  
735 those of Ciomadul has been observed in other volcanic systems. For instance, Nevado de  
736 Toluca (Mexico) experienced an eruption at  $\sim 13$  ka where biotite, up to 4 Ma old, was  
737 incorporated and resided in the magma for only a short period of time before it erupted  
738 (Arce et al. 2006). One can note that in this example, as well as at Ciomadul, mafic-  
739 intermediate magma replenished the system since  $\sim 1$  Ma and contributed to the eruption  
740 of new domes as well as effusive-explosive activity (Torres-Orozco et al., 2017a).

741         From amphibole thermobarometrical studies, Kiss et al. (2014) suggested a complex  
742 and multi-zonal context of polybaric crystallization of amphibole in the mid- to upper crust  
743 beneath Ciomadul. Crystallisation of these minerals occurred in a long-lived shallow storage  
744 zone (possibly shared with the neighbouring Pilișca volcano) filled with a cold crystal mush

745 (Kiss et al. 2014) that was subsequently remobilized by the injection of a hot mafic magma,  
746 as observed at Unzen, Montserrat or Ruapehu volcanoes (Nakamura 1995; Murphy et al.  
747 2000; Gamble et al. 2003).

748         Repose periods as long as those occurring between Ciodamul eruptions are frequently  
749 observed at these volcanoes fed by intermediate magmas. Illustrated by zircon  
750 crystallization ages ranging from 10s to 100s of thousands of years, these volcanoes have  
751 experienced prolonged and recurrent presence of melt-bearing magma (Cooper and Reid  
752 2008; Schmitt et al. 2010; Reid et al. 2011; Rubin et al. 2016). The operation of such volcanic  
753 plumbing systems generates a large amount of glomerocrystic aggregates made up of  
754 minerals, which begin to store radiogenic argon prior to eruption. At Ciomadul, at the depth  
755 of 8-12 km proposed by Kiss et al. (2014), the expected crystal-mush temperatures (240 –  
756 300 °C) are in the same order of magnitude as the closure temperature for argon gas in the  
757 mineral constituting the crystal clots: ~ 225-300 °C for plagioclase, ~ 350 °C for biotite and K-  
758 feldspar, and ~ 600 °C for hornblende ( assuming a cooling rate of 10°C/Ma; e.g. McDougall  
759 and Harrison, 1999; Cassata et al., 2009; Baxter, 2010). Consequently, these minerals likely  
760 began to store radiogenic argon in the crystal mush prior to the eruption. The newly injected  
761 magma batches of Ciomadul's eruptions, provided the heat to remobilise the crystal mush  
762 and its constituent mineral phases that had crystallised earlier from an evolved (silica-rich)  
763 magma. The biotite ages are significantly younger than those obtained on plagioclase and  
764 amphibole (Fig. 9). This can be interpreted as reflecting either a difference in the crystal clot  
765 ages from which the mineral originated (younger for biotite than plagioclase/amphibole).  
766 Alternatively, it may reflect a different behaviour of these minerals which come from a single  
767 source but which have a contrasting response to argon degassing when they are in contact  
768 with the replenishing magma. The former hypothesis is more speculative as incorporation of

769 xenocrysts would include all mineral phases present in the crystal mush without segregation,  
770 whereas the latter is easily obtained by consideration of diffusion processes.

771 The coexistence of hornblende and plagioclase in the crystal clots support the  
772 interpretation that the xenocrysts came from the same-aged source, and the diffusional Ar  
773 loss model implies a complete reset of radiogenic argon in the plagioclases (Gardner et al.,  
774 2002). Such results from the 74 ka Toba Tuff were interpreted incompatible with a long  
775 storage of xenocrystic minerals in the magma reservoir but, instead, were explained by  
776 contamination of the plutonic crystals, preceding the eruption by only a few years (Gardner  
777 et al. 2002). Models of diffusion in similar contexts (Gansecki et al. 1996; Gardner et al.  
778 2002; Bachmann et al. 2007) suggest that the magma of most Ciomadul monogenetic domes  
779 assimilated the solidified and cooled crystal-mush material (with trapped argon) shortly  
780 before extrusion. Consequently, the more than doubling of the xenocryst volume in the  
781 Ciomadul lava domes with time (from an average of 7% at 700 ka to ~ 17% at 60 ka, Fig. 11)  
782 can be interpreted as increasing assimilation of crystal mush, as it became increasingly  
783 fragmented and remobilised (Fig. 11).

#### 784 6.5 Geochemical evolution of the Ciomadul lava domes

785 With regard to the new geochronological constraints, we can consider the main  
786 petrological and geochemical features of magma evolution through time. Samples with ages  
787 > 450 ka seem to be characterized by a higher concentration (~23 vol.%) of plagioclase  
788 crystals, whereas their concentration slightly decreases toward the younger domes (~ 15 %)  
789 (Fig. 11). This can be attributed to shorter magmatic storage for the progressively younger  
790 rocks, limiting the growth of large plagioclase phenocrysts. On the other hand, over the 700

791 ky long history of Ciomadul's effusive volcanism, the proportion of xenocrysts or  
792 glomerocrystic aggregates slightly increases with time (Fig. 11).

793 While small groundmass microlites grew from their carrier liquid during the final phase  
794 of pre-eruptive or post-eruptive crystallization, large glomerocrysts were entrained from a  
795 crystal mush. Material erupted in later episodes contains proportionally more mush-derived  
796 material (Fig. 11), in relation to a larger amount of assimilation of the silicic crystal mush  
797 located beneath the volcano (cf. Kiss et al., 2014). Changes in phase proportions (Table 4 and  
798 Fig. 11) between Ciomadul eruptions highlight an increase of the glomerocryst entrainment  
799 efficiency during the whole Ciomadul history. With time, the proportion of crystal mush,  
800 fragmented during interaction with the new magma, increases. This induces an increasing  
801 mobility of the glomerocrysts, allowing them to be more readily remobilised, and eventually  
802 assimilated, during the injection of fresh magma. Such a scenario would explain the  
803 inherited argon increase through time as more and more inherited crystals are incorporated  
804 into the magma reaching the surface (Fig. 11).

805 Since 250 ka (i.e. over the main phase of Ciomadul dome activity), a temporal  
806 evolution in major element oxide concentrations can be seen (Fig. 12). With time, SiO<sub>2</sub> and  
807 Na<sub>2</sub>O concentrations significantly increase, as does, to a lesser extent, K<sub>2</sub>O. On the other  
808 hand, elements such as Fe<sub>2</sub>O<sub>3</sub>, MgO, as well as Al<sub>2</sub>O<sub>3</sub>, CaO and TiO<sub>2</sub> concentrations slightly  
809 decrease. The evolution through time for these oxides highlights the effect of fractional  
810 crystallization and the increase of the influence of crystal mush assimilation since 250 ka.  
811 The relatively good correlation between the degree of differentiation and time, as well as  
812 the general trends in the major element data, support a dual control by crystal-melt  
813 fractionation and crystal mush assimilation. Slightly decreasing of the plagioclase content  
814 through time as well as the concentrations of CaO and Al<sub>2</sub>O<sub>3</sub> could be considered as

815 paradoxical. However, geochemical data provided here are from whole-rock, i.e. from  
816 crystal-rich lavas where both plagioclase phenocrysts and xenocrysts influence element  
817 oxide concentration. Consequently, the total concentration of plagioclase (phenocryst +  
818 xenocryst) present in the lavas increases through time, which is in accordance with the  
819 expected behaviour of CaO and Al<sub>2</sub>O<sub>3</sub>.

## 820 **7 Conclusions**

821 New unspiked K-Ar dates acquired mostly from the groundmass of lava samples,  
822 complemented by major elements geochemistry, provide new insights into the  
823 geochronological evolution of the extrusive history of the Late Quaternary Ciomadul  
824 volcano. Our dating effort mainly focused on the central, most voluminous, part of  
825 Ciomadul, which was hitherto poorly constrained. Following a rigorous process of sample  
826 selection and preparation by a two-step separation, we managed to obtain groundmass  
827 aliquots avoiding any traces of xenocrysts. Most ages obtained on these groundmass  
828 fractions contradict those obtained by whole-rock K-Ar dating reported in previous studies  
829 and largely agree with (U-Th)-He ages. Based on the new results, the timing of the extrusive  
830 activity at Ciomadul can be summarised as follows: 1) a first stage from ca. 850 ka to 440 ka  
831 during which minor extrusive activity occurred in the area of the Puturosu Hills; followed by  
832 2) a shorter but more voluminous second stage from ca. 200 ka to 30 ka. During this second  
833 stage, volcanism began (between ca. 200 ka to 130 ka) when the northern and western-  
834 central parts of Ciomadul were constructed. Then, after a few tens of thousands of years of  
835 quiescence, predominantly effusive activity resumed at ~ 100 ka when the eastern-central  
836 part of the dome complex grew. This second phase of activity partly overlapped with the  
837 final, highly explosive eruptive phase that began at ~ 51 ka and ended around 29 ka

838 (Karátson et al. 2016). As the current quiescence period of the volcano is shorter than  
839 quiescence periods occurring in its earlier history, Ciomadul cannot be considered extinct.

840 In addition to the groundmass ages presented here, dating efforts focussing on pure  
841 mineral phases highlight that a large amount of inherited argon is responsible for the  
842 obvious shift from the systematically older whole-rock to the younger groundmass ages,  
843 showing a more or less linear relationship between excess argon and the abundance of  
844 inherited crystals. These crystals are more abundant in the younger rocks, indicating  
845 increasing contamination of magma by inherited crystals from a crystal mush during volcanic  
846 activity at Ciomadul. Some of the inherited crystals must have formed up to 2 Ma ago and  
847 may be associated with the neighbouring Pilișca volcano. Such a dual source of composition  
848 for the erupted material is noticeable on the kinked CSD plots of the Ciomadul dacitic lavas.  
849 Contrasting behaviour of the mineral phases during partial degassing inside the crystal mush,  
850 from their formation to the eruption and during their incorporation into the juvenile magma,  
851 can explain the wide range of ages obtained in a single sample. Comparison with the  
852 geochemical data suggests a magmatic evolution towards more SiO<sub>2</sub>-rich products and  
853 increasing assimilation and incorporation with time of an earlier-formed crystal mush.

854 In summary, Ciomadul's initial, sporadic dome extrusions in the SE of the volcanic  
855 complex were followed by much larger scale extrusive activity in the central part. The good  
856 spatial resolution of the obtained ages provides the basis for an assessment of magma  
857 extrusion volumes through time (Karátson et al., this volume). The rigorous sample  
858 preparation methodology, the small errors, and a complete analysis of all previously  
859 published radiometric ages, validates the reliability of the newly obtained K-Ar ages. This  
860 approach, when coupled with CSD and geochemical studies, demonstrates how such an

861 integrated approach can inform on the evolution of magmatic systems, the activity they  
862 feed, and the time scales of evolution over hundreds to hundreds-of-thousands of years

## 863 **Acknowledgements**

864 We wish to thank Karoly Nemeth and an anonymous reviewer, as well as Editors Stephen  
865 Self and Andrew Harris for their comments and suggestions, which greatly helped us to  
866 improve the clarity of the manuscript. This research was supported by the Hungarian  
867 Scientific Research Fund NKFIH - OTKA No. K 115472 to DK. Fruitful discussions with Carlos  
868 Palares and Xavier Quidelleur at different stages of this study have helped to clarify the ideas  
869 presented in this paper. This is Laboratoire de Géochronologie Multi-Techniques (LGMT)  
870 contribution number 146.

## 871 **References**

- 872 Anderson A (1976) Magma mixing - petrological process and volcanological tool. *J Volcanol*  
873 *Geotherm Res* 1:3–33. doi: 10.1016/0377-0273(76)90016-0
- 874 Arce JL, Macias JL, Gardner JE, Layer PW (2006) A 2.5 ka history of dacitic magmatism at  
875 Nevado de Toluca, Mexico: Petrological, Ar-40/Ar-39 dating, and experimental  
876 constraints on petrogenesis. *J Petrol* 47:457–479. doi: 10.1093/petrology/egi082
- 877 Armienti P, Pareschi M, Innocenti F, Pompilio M (1994) Effects of magma storage and ascent  
878 on the kinetics of crystal-growth - the case of the 1991-93 Mt Etna eruption. *Contrib*  
879 *Mineral Petrol* 115:402–414. doi: 10.1007/BF00320974
- 880 Bachmann O, Bergantz GW (2004) On the origin of crystal-poor rhyolites: Extracted from  
881 batholithic crystal mushes. *J Petrol* 45:1565–1582. doi: 10.1093/petrology/egh019
- 882 Bachmann O, Oberli F, Dungan MA, et al (2007) (40)Ar/(39)Ar and U-Pb dating of the Fish  
883 Canyon magmatic system, San Juan Volcanic field, Colorado: Evidence for an  
884 extended crystallization history. *Chem Geol* 236:134–166. doi:  
885 10.1016/j.chemgeo.2006.09.005
- 886 Balogh K, Nemeth K (2005) Evidence for the neogene small-volume intracontinental.  
887 volcanism in western hungary: K/Ar geochronology of the Tihany Maar volcanic  
888 complex. *Geol Carpathica* 56:91–99

- 889 Balogh K, Nemeth K, Itaya T, et al (2010) Loss of Ar-40(rad) from leucite-bearing basanite at  
890 low temperature: implications on K/Ar dating. *Cent Eur J Geosci* 2:385–398. doi:  
891 10.2478/v10085-010-0026-3
- 892 Baxter EF (2010) Diffusion of Noble Gases in Minerals. In: Zhang YX, Cherniak DJ (eds)  
893 Diffusion in Minerals and Melts. pp 509–557
- 894 Blake S (1990) Viscoplastic models of lava domes
- 895 Boven A, Pasteels P, Kelley SP, et al (2001) Ar-40/Ar-39 study of plagioclases from the  
896 Rogaland anorthosite complex (SW Norway); an attempt to understand argon ages in  
897 plutonic plagioclase. *Chem Geol* 176:105–135. doi: 10.1016/S0009-2541(00)00372-7
- 898 Brown SJA, Fletcher IR (1999) SHRIMP U-Pb dating of the preeruption growth history of  
899 zircons from the 340 ka Whakamaru Ignimbrite, New Zealand: Evidence for > 250 k.y.  
900 magma residence times. *Geology* 27:1035–1038. doi: 10.1130/0091-  
901 7613(1999)027<1035:SUPDOT>2.3.CO;2
- 902 Brown SJA, Wilson CJN, Cole JW, Wooden J (1998) The Whakamaru group ignimbrites, Taupo  
903 Volcanic Zone, New Zealand: evidence for reverse tapping of a zoned silicic magmatic  
904 system. *J Volcanol Geotherm Res* 84:1–37. doi: 10.1016/S0377-0273(98)00020-1
- 905 Cadoux A, Pinti DL, Aznar C, et al (2005) New chronological and geochemical constraints on  
906 the genesis and geological evolution of Ponza and Palmarola Volcanic Islands  
907 (Tyrrhenian Sea, Italy). *LITHOS* 81:121. doi: 10.1016/j.lithos.2004.09.020
- 908 Calvert AT, Moore RB, McGeehin JP, Rodrigues da Silva AM (2006) Volcanic history and Ar-  
909 40/Ar-39 and C-14 geochronology of Terceira Island, Azores, Portugal. *J Volcanol*  
910 *Geotherm Res* 156:103–115. doi: 10.1016/j.jvolgeores.2006.03.016
- 911 Cassata WS, Renne PR, Shuster DL (2009) Argon diffusion in plagioclase and implications for  
912 thermochronometry: A case study from the Bushveld Complex, South Africa.  
913 *Geochim Cosmochim Acta* 73:6600–6612. doi: 10.1016/j.gca.2009.07.017
- 914 Cassagnol C, Gillot P-Y (1982) Range and effectiveness of unspiked potassium-argon dating:  
915 experimental groundwork and applications. In: Numerical Dating in Stratigraphy,  
916 John Wiley & Sons. Odin G.S., pp 159–179
- 917 Cole JW, Deering CD, Burt RM, et al (2014) Okataina Volcanic Centre, Taupo Volcanic Zone,  
918 New Zealand: A review of volcanism and synchronous pluton development in an  
919 active, dominantly silicic caldera system. *Earth-Sci Rev* 128:1–17. doi:  
920 10.1016/j.earscirev.2013.10.008
- 921 Condit CD, Connor CB (1996) Recurrence rates of volcanism in basaltic volcanic fields: An  
922 example from the Springerville volcanic field, Arizona. *Geol Soc Am Bull* 108:1225–  
923 1241. doi: 10.1130/0016-7606(1996)108<1225:RROVIB>2.3.CO;2

- 924 Connor CB, Hill BE (1995) 3 nonhomogeneous Poisson models for the probability of basaltic  
925 volcanism - application to the Yucca Mountain region, Nevada. *J Geophys Res-Solid*  
926 *Earth* 100:10107–10125. doi: 10.1029/95JB01055
- 927 Cooper KM, Reid MR (2008) Uranium-series Crystal Ages. In: Putirka KD, Tepley FJ (eds)  
928 *Minerals, Inclusions and Volcanic Processes*. pp 479–544
- 929 Coulie E, Quidelleur X, Gillot PY, et al (2003) Comparative K-Ar and Ar/Ar dating of Ethiopian  
930 and Yemenite Oligocene volcanism: implications for timing and duration of the  
931 Ethiopian traps. *Earth Planet Sci Lett* 206:477–492. doi: 10.1016/S0012-  
932 821X(02)01089-0
- 933 Crisp J (1984) Rates of magma emplacement and volcanic output. *J Volcanol Geotherm Res*  
934 20:177–211. doi: 10.1016/0377-0273(84)90039-8
- 935 Dalrymple G, Moore J (1968) Argon-40 - excess in submarine pillow basalts from Kilauea  
936 volcano Hawaii. *Science* 161:1132-+. doi: 10.1126/science.161.3846.1132
- 937 Damaschke M, Cronin SJ, Bebbington MS (2018) A volcanic event forecasting model for  
938 multiple tephra records, demonstrated on Mt. Taranaki, New Zealand. *Bull Volcanol*  
939 80:9. doi: 10.1007/s00445-017-1184-y
- 940 Danisik M, Shane P, Schmitt AK, et al (2012) Re-anchoring the late Pleistocene  
941 tephrochronology of New Zealand based on concordant radiocarbon ages and  
942 combined U-238/Th-230 disequilibrium and (U-Th)/He zircon ages. *Earth Planet Sci*  
943 *Lett* 349:240–250. doi: 10.1016/j.epsl.2012.06.041
- 944 Dodson MH (1973) Closure temperature in cooling geochronological and petrological  
945 systems. *Contrib Mineral Petrol* 40:259–274. doi: 10.1007/BF00373790
- 946 Doherty AL, Bodnar RJ, De Vivo B, et al (2012) Bulk rock composition and geochemistry of  
947 olivine-hosted melt inclusions in the Grey Porri Tuff and selected lavas of the Monte  
948 dei Porri volcano, Salina, Aeolian Islands, southern Italy. *Cent Eur J Geosci* 4:338–355.  
949 doi: 10.2478/s13533-011-0066-7
- 950 Farley KA, Kohn BP, Pillans B (2002) The effects of secular disequilibrium on (U-Th)/He  
951 systematics and dating of Quaternary volcanic zircon and apatite. *Earth Planet Sci*  
952 *Lett* 201:117–125. doi: 10.1016/S0012-821X(02)00659-3
- 953 Gamble JA, Price RC, Smith IEM, et al (2003) Ar-40/Ar-39 geochronology of magmatic  
954 activity, magma flux and hazards at Ruapehu volcano, Taupo Volcanic Zone, New  
955 Zealand. *J Volcanol Geotherm Res* 120:271–287. doi: 10.1016/S0377-0273(02)00407-  
956 9
- 957 Gansecki CA, Mahood GA, McWilliams MO (1996) Ar-40/Ar-39 geochronology of rhyolites  
958 erupted following collapse of the Yellowstone caldera, Yellowstone Plateau volcanic  
959 field: Implications for crustal contamination. *Earth Planet Sci Lett* 142:91–107. doi:  
960 10.1016/0012-821X(96)00088-X

- 961 Gardner JE, Layer PW, Rutherford MJ (2002) Phenocrysts versus xenocrysts in the youngest  
962 Toba Tuff: Implications for the petrogenesis of 2800 km<sup>3</sup> of magma. *Geology*  
963 30:347–350. doi: 10.1130/0091-7613(2002)030<0347:PVXITY>2.0.CO;2
- 964 Germa A, Lahitte P, Quidelleur X (2015) Construction and destruction of Mont Pelee volcano:  
965 Volumes and rates constrained from a geomorphological model of evolution. *J*  
966 *Geophys Res-Earth Surf* 120:1206–1226. doi: 10.1002/2014JF003355
- 967 Germa A, Quidelleur X, Labanieh S, et al (2010) The eruptive history of Morne Jacob volcano  
968 (Martinique Island, French West Indies): Geochronology, geomorphology and  
969 geochemistry of the earliest volcanism in the recent Lesser Antilles arc. *J Volcanol*  
970 *Geotherm Res* 198:297–310. doi: 10.1016/j.jvolgeores.2010.09.013
- 971 Germa A, Quidelleur X, Labanieh S, et al (2011a) The volcanic evolution of Martinique Island:  
972 Insights from K-Ar dating into the Lesser Antilles arc migration since the Oligocene. *J*  
973 *Volcanol Geotherm Res* 208:122–135. doi: 10.1016/j.jvolgeores.2011.09.007
- 974 Germa A, Quidelleur X, Lahitte P, et al (2011b) The K-Ar Cassinot-Gillot technique applied to  
975 western Martinique lavas: A record of Lesser Antilles arc activity from 2 Ma to Mount  
976 Pelee volcanism. *Quat Geochronol* 6:341–355. doi: 10.1016/j.quageo.2011.02.001
- 977 Gertisser R, Charbonnier SJ, Keller J, Quidelleur X (2012) The geological evolution of Merapi  
978 volcano, Central Java, Indonesia. *Bull Volcanol* 74:1213–1233. doi: 10.1007/s00445-  
979 012-0591-3
- 980 Gillot P-Y, Cornette Y (1986) The Cassinot technique for potassium - argon dating, precision  
981 and accuracy - examples from the late Pleistocene to recent volcanics from southern  
982 Italy. *Chem Geol* 59:205–222
- 983 Gillot P-Y, Cornette Y, Max N, Floris B (1992) Two reference materials, trachytes MDO-G and  
984 ISH-G, for argon dating (KeAr and 40Ar/39Ar) of Pleistocene and Holocene rocks.  
985 *Geostand Newsl* 16:55–60. doi: 10.1111/j.1751-908X.1992.tb00487.x
- 986 Gillot P-Y, Hildenbrand A, Lefevre JC, Albore-Livadie C (2006) The K/Ar dating method:  
987 principle, analytical techniques, and application to Holocene volcanic eruptions in  
988 southern Italy. *Acta Vulcanol* 18:55–66
- 989 Gomez-Tuena A, LaGatta AB, Langmuir CH, et al (2003) Temporal control of subduction  
990 magmatism in the eastern Trans-Mexican Volcanic Belt: Mantle sources, slab  
991 contributions, and crustal contamination. *Geochem Geophys Geosystems* 4:8912.  
992 doi: 10.1029/2003GC000524
- 993 Gomez-Tuena A, Mori L, Goldstein SL, Perez-Arvizu O (2011) Magmatic diversity of western  
994 Mexico as a function of metamorphic transformations in the subducted oceanic  
995 plate. *Geochim Cosmochim Acta* 75:213–241. doi: 10.1016/j.gca.2010.09.029
- 996 Harangi S, Lenkey L (2007) Genesis of the Neogene to Quaternary volcanism in the  
997 Carpathian-Pannonian region: Role of subduction, extension, and mantle plume. In:

- 998 Beccaluva L, Bianchini G, Wilson M (eds) Cenozoic Volcanism in the Mediterranean  
999 Area. pp 67–92
- 1000 Harangi S, Lukács R, Schmitt AK, et al (2015a) Constraints on the timing of Quaternary  
1001 volcanism and duration of magma residence at Ciomadul volcano, east–central  
1002 Europe, from combined U–Th/He and U–Th zircon geochronology. *J Volcanol*  
1003 *Geotherm Res* 301:66–80. doi: 10.1016/j.jvolgeores.2015.05.002
- 1004 Harangi S, Molnár M, Vinkler AP, et al (2010) Radiocarbon dating of the last volcanic  
1005 eruptions of Ciomadul volcano, Southeast Carpathians, eastern-central Europe.  
1006 *Radiocarbon* 52:1498–1507
- 1007 Harangi S, Novák A, Kiss B, et al (2015b) Combined magnetotelluric and petrologic constrains  
1008 for the nature of the magma storage system beneath the Late Pleistocene Ciomadul  
1009 volcano (SE Carpathians). *J Volcanol Geotherm Res* 290:82–96. doi:  
1010 10.1016/j.jvolgeores.2014.12.006
- 1011 Harford C, Pringle MS, Sparks RSJ, Young SR (2002) The volcanic evolution of Montserrat  
1012 using  $^{40}\text{Ar}/^{39}\text{Ar}$  geochronology. In: *The Eruption of Soufrière Hills Volcano,*  
1013 *Montserrat, from 1995 to 1999, The Geological Society Memoirs.* Druitt, T.H.,  
1014 Kokelaar, B.P., London, pp 93–113
- 1015 Heizler MT, Perry FV, Crowe BM, et al (1999) The age of Lathrop Wells volcanic center: An  
1016  $\text{Ar-40}/\text{Ar-39}$  dating investigation. *J Geophys Res-Solid Earth* 104:767–804. doi:  
1017 10.1029/1998JB900002
- 1018 Higgins MD (1996) Crystal size distributions and other quantitative textural measurements in  
1019 lavas and tuff from Egmont volcano (Mt Taranaki), New Zealand. *Bull Volcanol*  
1020 58:194–204. doi: 10.1007/s004450050135
- 1021 Higgins MD (2002) Closure in crystal size distributions (CSD), verification of CSD calculations,  
1022 and the significance of CSD fans. *Am Mineral* 87:171–175
- 1023 Higgins MD (2006) Quantitative Textural Measurements in Igneous and Metamorphic  
1024 Petrology
- 1025 Higgins MD, Roberge J (2007) Three magmatic components in the 1973 eruption of Eldfell  
1026 volcano, Iceland: Evidence from plagioclase crystal size distribution (CSD) and  
1027 geochemistry. *J Volcanol Geotherm Res* 161:247–260. doi:  
1028 10.1016/j.jvolgeores.2006.12.002
- 1029 Hildenbrand A, Weis D, Madureira P, Marques FO (2014) Recent plate re-organization at the  
1030 Azores Triple Junction: Evidence from combined geochemical and geochronological  
1031 data on Faial, S.Jorge and Terceira volcanic islands. *Lithos* 210:27–39. doi:  
1032 10.1016/j.lithos2014.09.009
- 1033 Hildenbrand I Anthony; Gillot, Pierre-Yves; Le Roy (2004) Volcano-tectonic and geochemical  
1034 evolution of an oceanic intra-plate volcano: Tahiti-Nui (French Polynesia)

- 1035 Hofmann C, Feraud G, Courtillot V (2000) Ar-40/Ar-39 dating of mineral separates and whole  
1036 rocks from the Western Ghats lava pile: further constraints on duration and age of  
1037 the Deccan traps. *Earth Planet Sci Lett* 180:13–27. doi: 10.1016/S0012-  
1038 821X(00)00159-X
- 1039 Hora JM, Singer BS, Woerner G (2007) Volcano evolution and eruptive flux on the thick crust  
1040 of the Andean Central Volcanic Zone: Ar-40/Ar-39 constraints from Volcan  
1041 Parinacota, Chile. *Geol Soc Am Bull* 119:343–362. doi: 10.1130/B25954.1
- 1042 Huber C, Bachmann O, Dufek J (2011) Thermo-mechanical reactivation of locked crystal  
1043 mushes: Melting-induced internal fracturing and assimilation processes in magmas.  
1044 *Earth Planet Sci Lett* 304:443–454. doi: 10.1016/j.epsl.2011.02.022
- 1045 Karátson D, Telbisz T, Harangi S, et al (2013) Morphometrical and geochronological  
1046 constraints on the youngest eruptive activity in East-Central Europe at the Ciomadul  
1047 (Csomad) lava dome complex, East Carpathians. *J Volcanol Geotherm Res* 255:43–56.  
1048 doi: 10.1016/j.jvolgeores.2013.01.013
- 1049 Karátson D, Timár G (2005) Comparative volumetric calculations of two segments of the  
1050 Carpathian Neogene/Quaternary volcanic chain using SRTM elevation data:  
1051 implications for erosion and magma output rates. In: Thouret JC, Chester DK (eds)  
1052 *Volcanic Landforms, Processes and Hazards*. pp 19–35
- 1053 Karátson D, Wulf S, Veres D, et al (2016) The latest explosive eruptions of Ciomadul  
1054 (Csomad) volcano, East Carpathians - A tephrostratigraphic approach for the 51-29 ka  
1055 BP time interval. *J Volcanol Geotherm Res* 319:29–51. doi:  
1056 10.1016/j.jvolgeores.2016.03.005
- 1057 Kelley S (2002) Excess argon in K-Ar and Ar-Ar geochronology. *Chem Geol* 188:1–22. doi:  
1058 10.1016/S0009-2541(02)00064-5
- 1059 Kereszturi G, Bebbington M, Nemeth K (2017) Forecasting transitions in monogenetic  
1060 eruptions using the geologic record. *Geology* 45:283–286. doi: 10.1130/G38596.1
- 1061 Kersting AB, Arculus PJ (1994) Klyuchevskoy volcano, Kamchatka, Russia - the role of high-  
1062 flux recharged, tapped, and fractionated magma chamber(s) in the genesis of high-  
1063 AL<sub>2</sub>O<sub>3</sub> from high-MgO basalt. *J Petrol* 35:1–41
- 1064 Kis B-M, Ionescu A, Cardellini C, et al (2017) Quantification of carbon dioxide emissions of  
1065 Ciomadul, the youngest volcano of the Carpathian-Pannonian Region (Eastern-  
1066 Central Europe, Romania). *J Volcanol Geotherm Res* 341:119–130. doi:  
1067 10.1016/j.jvolgeores.2017.05.025
- 1068 Kiss B, Harangi S, Ntaflos T, et al (2014) Amphibole perspective to unravel pre-eruptive  
1069 processes and conditions in volcanic plumbing systems beneath intermediate arc  
1070 volcanoes: a case study from Ciomadul volcano (SE Carpathians). *Contrib Mineral  
1071 Petrol* 167:. doi: 10.1007/s00410-014-0986-6

- 1072 Lahitte P, Coulie E, Mercier N, et al (2001) K-Ar and TL volcanism chronology of the southern  
1073 ends of the Red Sea spreading in Afar since 300 ka. *Comptes Rendus Acad Sci Ser II*  
1074 *Fasc -Sci* 332:13–20. doi: 10.1016/S1251-8050(00)01491-9
- 1075 Lahitte P, Samper A, Quidelleur X (2012) DEM-based reconstruction of southern Basse-Terre  
1076 volcanoes (Guadeloupe archipelago, FWI): Contribution to the Lesser Antilles Arc  
1077 construction rates and magma production. *Geomorphology* 136:148–164. doi:  
1078 10.1016/j.geomorph.2011.04.008
- 1079 Lexa J, Seghedi I, Nemeth K, et al (2010) Neogene-Quaternary Volcanic forms in the  
1080 Carpathian-Pannonian Region: a review. *Cent Eur J Geosci* 2:207-U75. doi:  
1081 10.2478/v10085-010-0024-5
- 1082 Luhr JF, Allan J, Carmichael I, et al (1989) Primitive calc-alkaline and alkaline rock types from  
1083 the Western Mexican Volcanic Belt. *J Geophys Res-Solid Earth Planets* 94:4515–4530.  
1084 doi: 10.1029/JB094iB04p04515
- 1085 Marsh BD (1988) Crystal size distribution (CSD) in rocks and the kinetics and dynamics.  
1086 *Contrib Mineral Petrol* 99:277–291. doi: 10.1007/BF00375362
- 1087 Marzocchi W, Zaccarelli L (2006) A quantitative model for the time-size distribution of  
1088 eruptions. *J Geophys Res-Solid Earth* 111:B04204. doi: 10.1029/2005JB003709
- 1089 Matenco L, Bertotti G, Leever K, et al (2007) Large-scale deformation in a locked collisional  
1090 boundary: Interplay between subsidence and uplift, intraplate stress, and inherited  
1091 lithospheric structure in the late stage of the SE Carpathians evolution. *Tectonics*  
1092 26:TC4011. doi: 10.1029/2006TC001951
- 1093 Matthews NE, Pyle DM, Smith VC, et al (2012) Quartz zoning and the pre-eruptive evolution  
1094 of the similar to 340-ka Whakamaru magma systems, New Zealand. *Contrib Mineral*  
1095 *Petrol* 163:87–107. doi: 10.1007/s00410-011-0660-1
- 1096 McDougall I, Harrison TM (1999) *Geochronology and Thermochronology by the  $^{40}\text{Ar}/^{39}\text{Ar}$*   
1097 *Method*, 2nd edn; Oxford University Press, New York
- 1098 Mock A, Jerram DA (2005) Crystal size distributions (CSD) in three dimensions: Insights from  
1099 the. *J Petrol* 46:1525–1541. doi: 10.1093/petrology/egi024
- 1100 Molnár K, Harangi S, Lukács R, et al (2018) The onset of the volcanism in the Ciomadul  
1101 Volcanic Dome Complex (Eastern Carpathians): Eruption chronology and magma type  
1102 variation. *J Volcanol Geotherm Res*. doi:  
1103 <https://doi.org/10.1016/j.jvolgeores.2018.01.025>
- 1104 Morgan DJ, Jerram DA (2006) On estimating crystal shape for crystal size distribution  
1105 analysis. *J Volcanol Geotherm Res* 154:1–7. doi: 10.1016/j.jvolgeores.2005.09.016
- 1106 Moriya I, Okuno M, Nakamura T, et al (1996) Radiocarbon ages of charcoal fragments from  
1107 the pumice flow deposit of the last eruption of Ciomadul volcano, Romania. In:  
1108 *Summaries of Researches using AMS*. Nagoya University 7, pp 255–257

- 1109 Murphy MD, Sparks RSJ, Barclay J, et al (2000) Remobilization of andesite magma by  
1110 intrusion of mafic magma at the Soufriere Hills Volcano, Montserrat, West Indies. *J*  
1111 *Petrol* 41:21–42. doi: 10.1093/petrology/41.1.21
- 1112 Nakamura M (1995) Continuous mixing of crystal mush and replenished magma in the  
1113 ongoing Unzen eruption. *Geology* 23:807–810. doi: 10.1130/0091-  
1114 7613(1995)023<0807:CMOCMA>2.3.CO;2
- 1115 Neave DA, Buisman I, Maclennnnan J (2017) Continuous mush disaggregation during the  
1116 long-lasting Laki fissure eruption, Iceland. *Am Mineral* 102:2007–2021. doi:  
1117 10.2138/am-2017-6015CCBY
- 1118 Nemeth K, Kereszturi G (2015) Monogenetic volcanism: personal views and discussion. *Int J*  
1119 *Earth Sci* 104:2131–2146. doi: 10.1007/s00531-015-1243-6
- 1120 Nishimura K, Kawamoto T, Kobayashi T, et al (2005) Melt inclusion analysis of the Unzen  
1121 1991-1995 dacite: implications for crystallization processes of dacite magma. *Bull*  
1122 *Volcanol* 67:648–662. doi: 10.1007/s00445-004-0400-8
- 1123 Ozawa A, Tagami T, Kamata H (2006) Argon isotopic composition of some Hawaiian historical  
1124 lavas. *Chem Geol* 226:66–72. doi: 10.1016/j.chemgeo.2005.10.001
- 1125 Pécskay Z, Lexa J, Szakacs A, et al (1995) Space and time distribution of Neogene-Quaternary  
1126 volcanism in the Carpatho- Pannonian Region. *Acta Vulcanol* 7:15–28
- 1127 Pécskay Z, Lexa J, Szakacs A, et al (2006) Geochronology of Neogene magmatism in the  
1128 Carpathian arc and intra-Carpathian area. *Geol Carpathica* 57:511–530
- 1129 Pécskay Z, Szakács A, Seghedi I, Karátson D (1992) New data on the geochronological  
1130 interpretation of Cucu volcano and its environs (South Harghita, Romania). *Hung*  
1131 *Földt Közl* 122/2–4:265–286
- 1132 Peltz S, Vajdea E, Balogh K, Pécskay Z (1987) Contribution to the geochronological study of  
1133 the volcanic processes in the Calimani and Harghita Mts. In: *Contribution to the*  
1134 *geochronological study of the volcanic processes in the Calimani and Harghita Mts.*  
1135 *Dari S. Sed. Inst. Geol. Geofiz.* Volume, pp 323–338
- 1136 Popa M, Radulian M, Szakács A, et al (2012) New Seismic and Tomography Data in the  
1137 Southern Part of the Harghita Mountains (Romania, Southeastern Carpathians):  
1138 Connection with Recent Volcanic Activity. *Pure Appl Geophys* 169:1557–1573. doi:  
1139 10.1007/s00024-011-0428-6
- 1140 Quidelleur X, Gillot PY, Soler V, Lefevre JC (2001) K/Ar dating extended into the last  
1141 millennium: application to the youngest effusive episode of the Teide volcano  
1142 (Spain). *Geophys Res Lett* 28:3067–3070. doi: 10.1029/2000GL012821
- 1143 Rangel E, Arce JL, Macias JL (2018) Storage conditions of the similar to 29 ka rhyolitic  
1144 Guangoche White Pumice Sequence, Los Azufres Volcanic Field, Central Mexico. *J*  
1145 *Volcanol Geotherm Res* 358:132–148. doi: 10.1016/j.jvolgeores.2018.03.016

- 1146 Reid MR, Vazquez JA, Schmitt AK (2011) Zircon-scale insights into the history of a  
1147 Supervolcano, Bishop Tuff, Long Valley, California, with implications for the Ti-in-  
1148 zircon geothermometer. *Contrib Mineral Petrol* 161:293–311. doi: 10.1007/s00410-  
1149 010-0532-0
- 1150 Reyes-Guzman N, Siebe C, Chevrel MO, et al (2018) Geology and radiometric dating of  
1151 Quaternary monogenetic volcanism in the western Zacapu lacustrine basin  
1152 (Michoacan, Mexico): implications for archeology and future hazard evaluations. *Bull*  
1153 *Volcanol* 80:18. doi: 10.1007/s00445-018-1193-5
- 1154 Rubin A, Cooper KM, Leever M, et al (2016) Changes in magma storage conditions following  
1155 caldera collapse at Okataina Volcanic Center, New Zealand. *Contrib Mineral Petrol*  
1156 171:4. doi: 10.1007/s00410-015-1216-6
- 1157 Samper A, Quidelleur X, Komorowski J-C, et al (2009) Effusive history of the Grande  
1158 Decouverte Volcanic Complex, southern Basse-Terre (Guadeloupe, French West  
1159 Indies) from new K-Ar Cassignol-Gillot ages. *J Volcanol Geotherm Res* 187:117–130.  
1160 doi: 10.1016/j.jvolgeores.2009.08.016
- 1161 Samper A, Quidelleur X, Lahitte P, Mollex D (2007) Timing of effusive volcanism and collapse  
1162 events within an oceanic arc island: Basse-Terre, Guadeloupe archipelago (Lesser  
1163 Antilles Arc). *Earth Planet Sci Lett* 258:175–191. doi: 10.1016/j.epsl.2007.03.030
- 1164 Schimmelpfennig I, Benedetti L, Garreta V, et al (2011) Calibration of cosmogenic Cl-36  
1165 production rates from Ca and K spallation in lava flows from Mt. Etna (38 degrees N,  
1166 Italy) and Payun Matru (36 degrees S, Argentina). *Geochim Cosmochim Acta*  
1167 75:2611–2632. doi: 10.1016/j.gca.2011.02.013
- 1168 Schmitt AK, Stockli DF, Niedermann S, et al (2010) Eruption ages of Las Tres Virgenes volcano  
1169 (Baja California): A tale of two helium isotopes. *Quat Geochronol* 5:503–511. doi:  
1170 10.1016/j.quageo.2010.02.004
- 1171 Seghedi I, Matenco L, Downes H, et al (2011) Tectonic significance of changes in post-  
1172 subduction Pliocene-Quaternary magmatism in the south east part of the Carpathian-  
1173 Pannonian Region. *Tectonophysics* 502:146–157. doi: 10.1016/j.tecto.2009.12.003
- 1174 Shane P, Martin SB, Smith VC, et al (2007) Multiple rhyolite magmas and basalt injection in  
1175 the 17.7 ka Rerewhakaaitu eruption episode from Tarawera volcanic complex, New  
1176 Zealand. *J Volcanol Geotherm Res* 164:1–26. doi: 10.1016/j.jvolgeores.2007.04.003
- 1177 Singer BS, Thompson RA, Dungan MA, et al (1997) Volcanism and erosion during the past  
1178 930 ky at the Tataro San Pedro complex, Chilean Andes. *Geol Soc Am Bull* 109:127–  
1179 142. doi: 10.1130/0016-7606(1997)109<0127:VAEDTP>2.3.CO;2
- 1180 Singer BS, Wijbrans JR, Nelson ST, et al (1998) Inherited argon in a Pleistocene andesite lava:  
1181 <sup>40</sup>Ar/<sup>39</sup>Ar incremental-heating and laser-fusion analyses of plagioclase. *Geology*  
1182 26:427–430

- 1183 Smith VC, Shane P, Nairn IA (2004) Reactivation of a rhyolitic magma body by new rhyolitic  
1184 intrusion before the 15.8 ka Rotorua eruptive episode: implications for magma  
1185 storage in the Okataina Volcanic Centre, New Zealand. *J Geol Soc* 161:757–772. doi:  
1186 10.1144/0016-764903-092
- 1187 Smith VC, Shane P, Nairn IA (2005) Trends in rhyolite geochemistry, mineralogy, and magma  
1188 storage during the last 50 kyr at Okataina and Taupo volcanic centres, Taupo Volcanic  
1189 Zone, New Zealand. *J Volcanol Geotherm Res* 148:372–406. doi:  
1190 10.1016/j.jvolgeores.2005.05.005
- 1191 Steiger R, Jager E (1977) Subcommittee on geochronology - convention on use of decay  
1192 constants in geochronology and cosmochronology. *Earth Planet Sci Lett* 36:359–362.  
1193 doi: 10.1016/0012-821X(77)90060-7
- 1194 Stewart RB (2010) Andesites as Magmatic Liquids or Liquid-crystal Mixtures; Insights from  
1195 Egmont and Ruapehu Volcanoes, New Zealand. *Cent Eur J Geosci* 2:329–338. doi:  
1196 10.2478/v10085-010-0022-7
- 1197 Stipp J, McDougal I, Polach H (1969) Excess radiogenic argon in young subaerial basalts from  
1198 Auckland volcanic field New Zealand. *Trans-Am Geophys Union* 50:330+
- 1199 Szabo C, Harangi S, Csontos L (1992) Review Of Neogene And Quaternary Volcanism Of The  
1200 Carpathian Pannonian Region. *Tectonophysics* 208:243–256. doi: 10.1016/0040-  
1201 1951(92)90347-9
- 1202 Szakács A, Seghedi I (1995) The Călimani–Gurghiu–Harghita volcanic chain, East Carpathians,  
1203 Romania: volcanological features. *Acta Volcanol* 7:145–153
- 1204 Szakács A, Seghedi I, Pécskay Z (1993) Peculiarities of South Harghita Mts. as terminal  
1205 segment of the Carpathian Neogene to Quaternary volcanic chain. *Rev Roum Géol*  
1206 *Géophys Géogr Géol* 37:21–37
- 1207 Szakács A, Seghedi I, Pécskay Z, Mirea V (2015) Eruptive history of a low-frequency and low-  
1208 output rate Pleistocene volcano, Ciomadul, South Harghita Mts., Romania. *Bull*  
1209 *Volcanol* 77:. doi: 10.1007/s00445-014-0894-7
- 1210 Tanaka K, Shoemaker E, Ulrich G, Wolfe E (1986) Migration of volcanism in the San-Francisco  
1211 volcanic field, Arizona. *Geol Soc Am Bull* 97:129–141. doi: 10.1130/0016-  
1212 7606(1986)97<129:MOVITS>2.0.CO;2
- 1213 Tantau I, Reille M, de Beaulieu JL, et al (2003) Vegetation history in the Eastern Romanian  
1214 Carpathians: pollen analysis of two sequences from the Mohos crater. *Veg Hist*  
1215 *Archaeobotany* 12:113–125. doi: 10.1007/s00334-003-0015-6
- 1216 Torres-Orozco R, Arce JL, Layer PW, Benowitz JA (2017) The Quaternary history of effusive  
1217 volcanism of the Nevado de Toluca area, Central Mexico. *J South Am Earth Sci* 79:12–  
1218 39. doi: 10.1016/j.jsames.2017.07.008

- 1219 Turner MB, Bebbington MS, Cronin SJ, Stewart RB (2009) Merging eruption datasets:  
1220 building an integrated Holocene eruptive record for Mt Taranaki, New Zealand. Bull  
1221 Volcanol 71:903–918. doi: 10.1007/s00445-009-0274-x
- 1222 Turner MB, Cronin SJ, Bebbington MS, et al (2011) Integrating records of explosive and  
1223 effusive activity from proximal and distal sequences: Mt. Taranaki, New Zealand.  
1224 Quat Int 246:364–373. doi: 10.1016/j.quaint.2011.07.006
- 1225 Vaselli O, Minissale A, Tassi F, et al (2002) A geochemical traverse across the Eastern  
1226 Carpathians (Romania): constraints on the origin and evolution of the mineral water  
1227 and gas discharges. Chem Geol 182:637–654. doi: 10.1016/S0009-2541(01)00348-5
- 1228 Vinkler A, Harangi S, Ntaflou T, Szakács A (2007) Petrology and geochemistry of pumices from  
1229 the Ciomadul volcano (Eastern Carpathians)—implication for petrogenetic processes.  
1230 (in Hungarian with an English abstract). Foldtani Kozlony 103–128
- 1231 Wulf S, Fedorowicz S, Veres D, et al (2016) The “Roxolany Tephra” (Ukraine) - new evidence  
1232 for an origin from Ciomadul volcano, East Carpathians.” J Quat Sci 31:565–576. doi:  
1233 10.1002/jqs.2879
- 1234 Zellmer G, Turner S, Hawkesworth C (2000) Timescales of destructive plate margin  
1235 magmatism: new insights from Santorini, Aegean volcanic arc. Earth Planet Sci Lett  
1236 174:265–281. doi: 10.1016/S0012-821X(99)00266-6
- 1237 Zellmer GF, Sparks RSJ, Hawkesworth CJ, Wiedenbeck M (2003) Magma emplacement and  
1238 remobilization timescales beneath Montserrat: Insights from Sr and Ba zonation in  
1239 plagioclase phenocrysts. J Petrol 44:1413–1431. doi: 10.1093/petrology/44.8.1413
- 1240 Zimmerer MJ, Lafferty J, Coble MA (2016) The eruptive and magmatic history of the  
1241 youngest pulse of volcanism at the Valles caldera: Implications for successfully dating  
1242 late Quaternary eruptions. J Volcanol Geotherm Res 310:50–57. doi:  
1243 10.1016/j.jvolgeores.2015.11.021
- 1244

1245

1246 **Figure captions**

1247 Fig. 1 A) DEM in shaded relief of Eastern Carpathian; B) Location of the main East Carpathian  
1248 volcanic massifs; C) Ciomadul dome complex. Sample locations (squares) are color-coded  
1249 according to their sector: red squares: peripheral south-eastern and northern domes; green  
1250 squares: western-central part of the dome complex; purple squares: eastern-central part of  
1251 the dome complex. Ages and uncertainties are in ka. St. Ana and Mohoş: uneroded twin  
1252 craters.

1253 Fig. 2 Photomicrograph of a thin section of the Haramul Mare dome in plane-polarised (A)  
1254 and cross-polarised (B) view. Plag.: plagioclase; Biot.: biotite; Amp.: amphibole; Glom.:  
1255 glomerocrysts, mostly composed of plagioclase phenocrysts and small hornblende (Hb.),  
1256 appear in the upper part as a crystal clot. Width is 10 mm. C) Close-up view of the microlitic  
1257 groundmass and microphenocrysts.

1258 Fig. 3 Illustration of the procedure of the two-step sample separation from a  
1259 photomicrograph of sample 15CIO01. Mosaics b, c and d simulate the results of the  
1260 separation. Each square in these mosaics represents a fraction of the crushed sample that is  
1261 either kept (visible) or removed (hidden by green squares) during the separation. a) Thin  
1262 section in cross-polarised light (field of view is 8 mm wide). Labels highlight characteristic  
1263 anhedral glomerocryst (anh. glom.) and euhedral plagioclase (enh. plag.). b) Grains selected  
1264 by the first step. Note the small diamond-like phenocryst (at the center left), the peripheral  
1265 part of large phenocrysts, and the abundance of microphenocrysts (in the upper half) that  
1266 remain after this first step. c) Grains that remain selected after the second step of

1267 preparation. d) Grains that would not be removed from the groundmass in the case of a  
1268 single-step of separation.

1269 Fig. 4 Semi-log crystal size distribution (CSD) plots for mineral phases in the Ciomadul lava  
1270 dome A) Plagioclase (black curves) and mafic (amphibole and biotite, grey curves) crystal  
1271 CSD plot. All but those for sample 16C1O08 (coloured curves) show kinked profiles. Insets  
1272 show analysed micro-photographs used in the CSD plots in B) and C) (plagioclase in white,  
1273 mafic crystals in black, groundmass in grey) B) Fitting of a mixture of two magmas with linear  
1274 CSDs to the observed CSD from samples 16C1O01 and 15C1O09 for plagioclases focussed on  
1275 the kink zone between the two linear segments for the fine and coarse grains. Regressions  
1276 though coherent populations, for which assumptions of near-uniform morphologies are  
1277 valid, are shown as dotted lines. Values for the equation of these regressed lines and  $R^2$   
1278 values are given (same box colour as the corresponding line). Inset shows the complete CSD  
1279 graph. C) Same graph as B) but for mafic (biotite) crystals.

1280 Fig. 5 Graph comparing K-Ar results and those proposed in previous studies. Each dome on  
1281 this diagram is plotted according to the age obtained by this work (X-axis) vs. the age  
1282 obtained in previous studies (Y-axis). Error bars and black squares show  $2\sigma$  (95%) confidence  
1283 interval.

1284 Fig. 6 A)  $K_2O$  vs  $SiO_2$  diagram (Peccerillo and Taylor; 1976), for Ciomadul lava dome samples;  
1285 B) Harker diagrams showing the variations of major element oxides as a function of  $SiO_2$ .

1286 Fig. 7 Whole-rock age model from thin section analysis (sample 15C1O01, same as Fig. 3). a)  
1287 Upper left: Identification of the mineral phases by binarization; lower right: Mosaicing of  
1288 previous image to simulate 200  $\mu m$  grain size. b) Grain composition analysis from their  
1289 grayscale properties (converted to colour for easier identification). Yellow: pure plagioclase;

1290 blue: groundmass; shaded white to red to black: mixed grains with increasing proportion of  
1291 groundmass grains. c) Distribution of the grain density proportion (left Y-axis) and ages  
1292 modelled for each grain composition (dotted black curve scaled on the right Y-axis). Bottom  
1293 scale defines the expected density of the respective grain populations.

1294 Fig. 8 Graph of the inherited argon abundance (deduced from whole-rock ages) versus  
1295 abundance of glomerocrysts (in vol%). Heavy lines display a  $\pm 1\sigma$  correlation trend. Thin  
1296 horizontal lines are the estimation ( $\pm 1\sigma$ ) of inherited argon abundance for the Dealul Cetății  
1297 dome obtained from the analysis of its thin section in order to propose a corrected eruption  
1298 age.

1299 Fig. 9 Compilation of the ages obtained on groundmass and separated minerals. Samples are  
1300 sorted with respect to the distance to the ~2 Ma old Pilișca volcano.

1301 Fig. 10 Map of the ages (in ka) obtained from the different phases of the Dealul Cetății dome  
1302 (15CIO01). The small and large grids correspond to the two-step and single-step procedure,  
1303 respectively.

1304 Fig. 11 Graph of the evolution of abundance of phenocrysts, glomerocrysts (in vol% of dome,  
1305 on left axis) and amount of argon inherited from xenocrysts (in %, on right axis) versus  
1306 eruption age. Boxes show global trends for each parameter. Schematic cartoon summarizing  
1307 a scenario for the assimilation of xenocrysts by dacitic magma based on crystal mush  
1308 disaggregation and increasing incorporation of inherited crystals in juvenile magma trough  
1309 time (modified from Neave et al., 2017). The figures are not to scale.

1310 Fig. 12 Geochemical evolution of major element oxides (in wt. %) of dacitic domes of  
1311 Ciomadul through time (eruption ages in ka).

Table 1 CSD input parameters and results, including crystal habit and  $L_{\max}$ .

Sample	Mineral	Count	Crystal Habit				Shape	$L_{\max}$ (mm)	Phase proportion
			Short	Interm.	Long	$R^2$ values			
16CIO08	Plagioclase	8164	1	1.5	3	0.86	Tabular	2.93	35.2%
16CIO08	Mafic m.	5454	1	1.5	3	0.85	Columnar	1.58	12.3%
15CIO01	Plagioclase	3465	1	1.3	2.1	0.88	Tabular	4.20	29.5%
15CIO01	Mafic m.	2781	1	1.25	2.1	0.83	Columnar	1.39	7.9%
15CIO09	Plagioclase	5720	1	1.25	2.1	0.86	Tabular	4.79	38.0%
15CIO09	Mafic m.	2008	1	1.5	3	0.88	Columnar	2.08	11.3%
16CIO09	Plagioclase	3020	1	1.3	2.2	0.87	Tabular	4.31	33.7%
16CIO09	Mafic m.	3486	1	1.6	2.9	0.88	Columnar	1.55	7.4%

1009 Table 2 K-Ar ages obtained in this study for Ciomadul lava domes. (G.M.: groundmass; ; Plag.  $\mu$ P.: plagioclase microphenocrysts; D.S.: two-step  
 1010 separation; S.S.: single-step separation); Sample coordinates are projected using the Universal Transverse Mercator (UTM) projection (zone 35  
 1011 N).

stage	Sample code Dome Name	Easting (in m)	Northing (in m)	Eleva- tion (m asl)	Dated phase	Fraction Size ( $\mu$ m)	K%	$^{40}\text{Ar}^* \pm 1\sigma$ (in % of total $^{40}\text{Ar}$ )		$^{40}\text{Ar}^*$ relative uncertainty	$^{40}\text{Ar}^* \pm 1\sigma$ $\times 10^{11}$ at/g		Age $\pm 1\sigma$ (in ka)	Weighted mean age $\pm 1\sigma$	
1 <sup>st</sup> stage	16CIO08 Muntele Puturosu	418645	5107909	1099	G.M.	63-125	3.226	5.233	0.169	0.726%	23.29	0.885	691	17	
								4.489	0.108	0.446%	24.26	0.485	720	19	<b>704 <math>\pm</math> 18</b>
	16CIO07 Balvanyos	419620	5107472	846	G.M.	63-125	3.585	29.213	0.089	0.373%	23.78	2.592	635	10	
								34.293	0.065	0.268%	24.19	2.225	646	9	<b>641 <math>\pm</math> 9</b>
2 <sup>nd</sup> stage	16CIO06 Balvanyos	419673	5107443	856	G.M.	63-125	3.449	4.283	0.043	0.280%	15.45	0.185	429	12	
								4.488	0.101	0.624%	16.24	0.455	451	12	<b>440 <math>\pm</math> 12</b>
	16CIO01 Haramul Mic	416986	5114107	866	Plag. $\mu$ P.	63-125	1.336	1.025	0.201	6.438%	3.127	0.206	224	26	
								1.211	0.076	2.065%	3.680	0.092	264	23	<b>245 <math>\pm</math> 24</b>
	15CIO01 Dealul Cetății	413713	5110905	994	G.M.	63-125	3.722	4.399	0.084	1.182%	7.139	0.371	184	5	
								4.170	0.075	1.055%	7.132	0.314	183	5	<b>184 <math>\pm</math> 5</b>
	16CIO02 Vârful Comlos	413146	5109912	1242	G.M.	63-125	3.471	4.266	0.055	1.055%	5.220	0.235	144	4	
								4.234	0.016	0.307%	5.209	0.068	144	4	<b>144 <math>\pm</math> 4</b>
16CIO04 Ciomadul Mare	413873	5109760	1260	Plag. $\mu$ P.	40-80	1.391	1.209	0.029	1.655%	1.725	0.034	119	10		
							1.508	0.049	2.322%	2.102	0.074	145	10	<b>133 <math>\pm</math> 18</b>	
15CIO09 Haramul Mare	416664	5111953	902	G.M.	63-125	3.668	6.414	0.042	1.107%	3.754	0.267	98	2		
							12.020	0.073	2.005%	3.639	0.877	95	2	<b>96 <math>\pm</math> 2</b>	
16CIO09 Piscul Pietros	415362	5108313	1101	G.M.	63-125	3.441	1.162	0.058	2.840%	2.042	0.067	57	5		
							1.323	0.063	2.797%	2.239	0.083	62	5	<b>60 <math>\pm</math> 5</b>	

1012

1015 Table 3 Major element concentrations for the Ciomadul lava domes (in wt%%).

Sample	15CIO09	16CIO01	16CIO02	16CIO03	16CIO04	16CIO05	16CIO06	16CIO07	16CIO08	16CIO09	16CIO11
SiO <sub>2</sub>	65.26	66.18	66.59	65.60	66.87	66.50	61.80	61.74	64.68	67.07	67.36
TiO <sub>2</sub>	0.45	0.35	0.38	0.37	0.32	0.32	0.52	0.53	0.53	0.31	0.29
Al <sub>2</sub> O <sub>3</sub>	16.85	16.46	16.62	16.62	16.29	16.20	17.35	17.43	17.82	16.15	16.26
Fe <sub>2</sub> O <sub>3</sub>	2.86	2.41	2.47	2.51	2.28	2.28	3.54	3.65	2.22	2.11	1.99
MnO	0.06	0.05	0.05	0.05	0.05	0.05	0.07	0.07	0.04	0.05	0.04
MgO	1.93	1.54	1.64	1.67	1.52	1.51	2.18	2.22	1.33	1.39	1.32
CaO	4.03	3.55	3.66	3.65	3.22	3.26	4.78	4.94	3.56	3.00	2.89
Na <sub>2</sub> O	4.34	4.07	4.34	4.24	4.30	4.31	4.22	4.33	4.36	4.43	4.67
K <sub>2</sub> O	3.36	3.46	3.32	3.21	3.61	3.57	3.40	3.20	3.28	3.55	3.50
P <sub>2</sub> O <sub>5</sub>	0.20	0.12	0.16	0.14	0.13	0.14	0.18	0.18	0.13	0.11	0.12
LOI	0.3	1.5	0.4	1.6	1.1	1.5	1.6	1.3	1.6	1.5	1.2
Sum	99.64	99.69	99.63	99.66	99.69	99.64	99.64	99.59	99.55	99.67	99.64

1016

1017 Table 4 Comparison between new and previously proposed ages. For each dated dome, abundance (in vol%) are given for: K-bearing minerals  
 1018 (P.: plagioclase; B.: biotite; A.: amphibole), total of K-bearing phenocrysts (T. Ph.); glomerocrysts (Glom.); and groundmass (G.M.); W.-R. Age:  
 1019 previously proposed age on whole-rock for the same lava dome;  $Ar_{inherited}$ : fraction (in %) of the total of radiogenic argon assumed to be inherited;  
 1020 Source: references for whole rock and (U–Th)/He ages: 1: Casta (1980); 2: Pécskay et al. (1992); 3: Pécskay et al. (1995b); 4: Karátson et al.,  
 1021 (2013); 5 : Szakács et al. (2015); 6: Harangi et al. (2015b); 7: Molnár et al. (2018); 8: this work

Location	New measurements (this work)								Previously proposed ages				
	Sample	Cassignol-Gillot (unspike) method			T. Ph. vol%	Glom. vol%	G.M. vol%	Age (in ka)	Traditional K-Ar method			(U–Th)/He method	
		P.	B.	A.					W.-R. age	Sour- ce	$Ar_{inherited}$ (%)	(U–Th)/He Age	Sour- ce
Puturosul	16CIO08	19	2	5	26	1	65	704 ± 18	710 ± 50	5	1 ± 7	642 ± 44	7
Bálványos	16CIO07	25	3	8	36	14	39	641 ± 9	1020 ± 150	3	37 ± 16	583 ± 30	7
Bálványos	16CIO06	23	1	7	31	13	47	440 ± 12	920 ± 180	3	52 ± 22		
Haramul Mic	16CIO01	10	2	7	19	18	54	245 ± 24	850 ± 200	1	71 ± 29	154 ± 16	7
Dealul Cetății	15CIO01	11	2	6	19	17	56	184 ± 5	400 ± 160	5	54 ± 45	116 – 142	4
Haramul Mare	15CIO09	12	4	6	22	16	44	96 ± 2	590 ± 160	3			
									231 ± 5	8	58 ± 3		
Piscul Pietros	16CIO09	21	2	8	30	23	47	60 ± 5	560 ± 110	2	89 ± 26	42.9 ± 1.5	6
Vârful Comlos	16CIO02	14	2	8	22	8	59	144 ± 4					
Ciomadul Mare	16CIO04	22	2	10	34	13	41	133 ± 18					

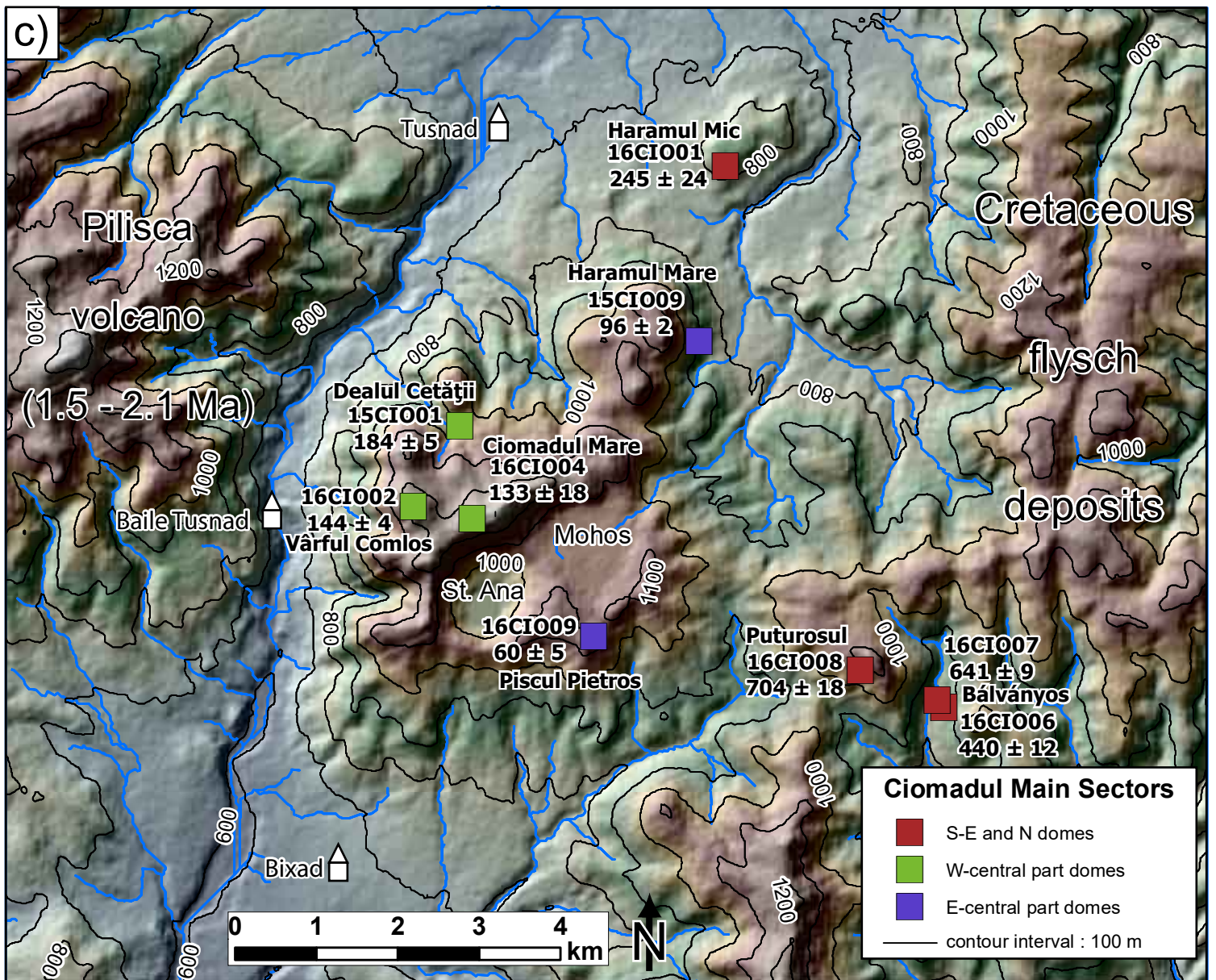
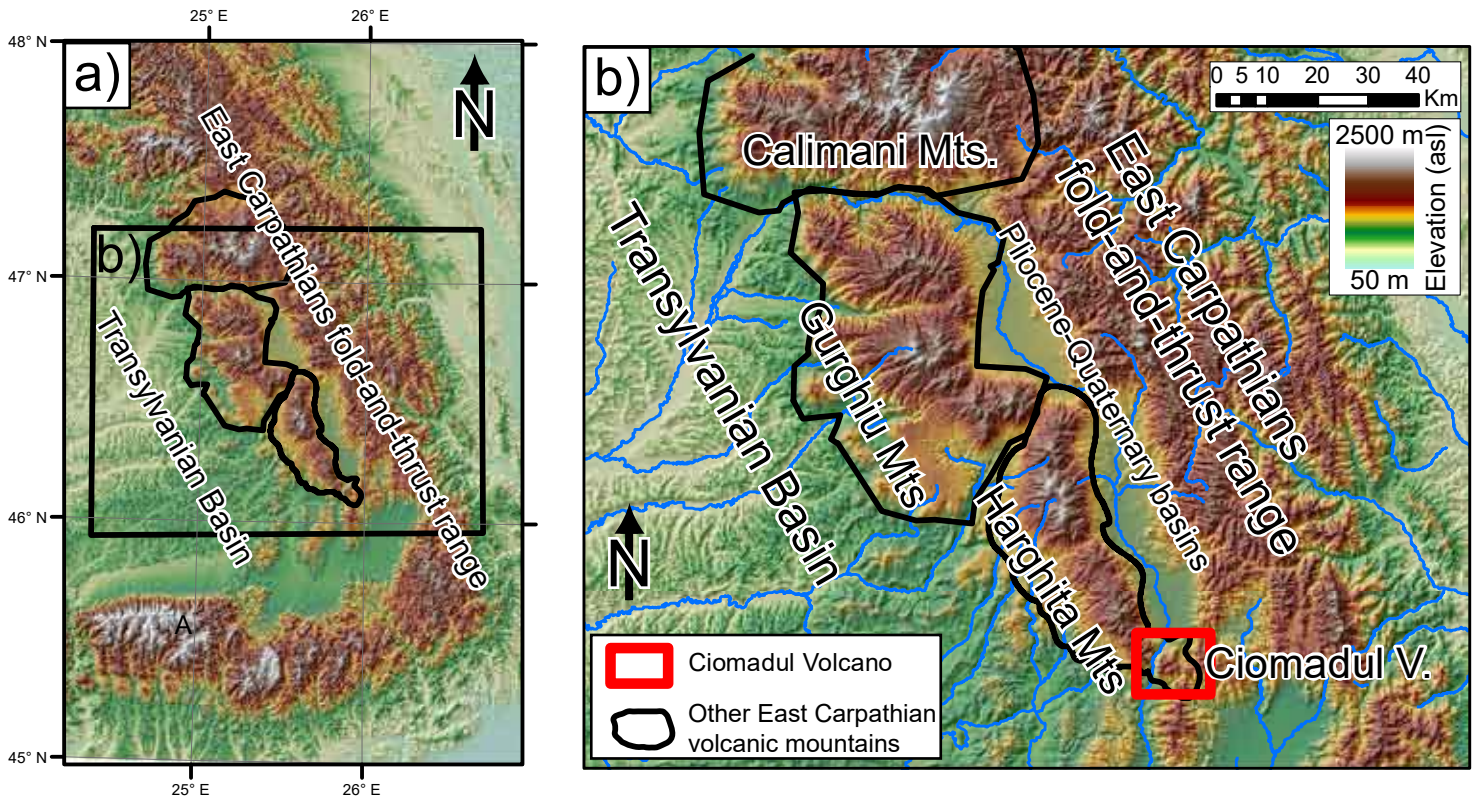
1023 Table 5 K-Ar ages obtained on separated pure phases, larger grain size groundmass, and whole rock. Dated phases: Amp.: Amphibole; Biot.:

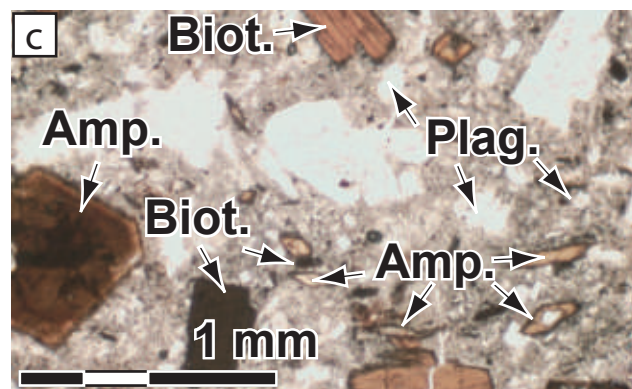
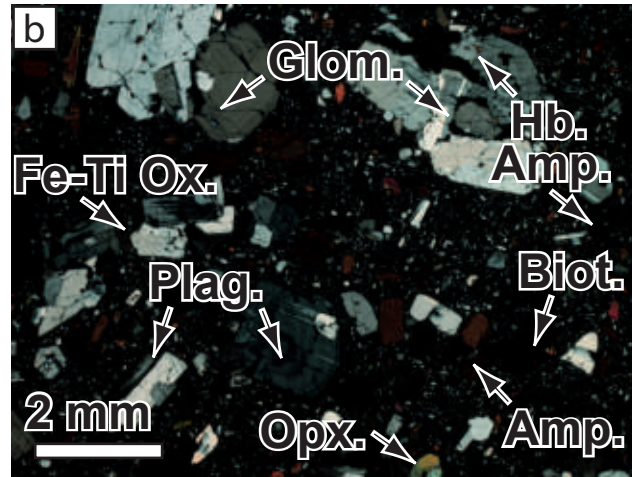
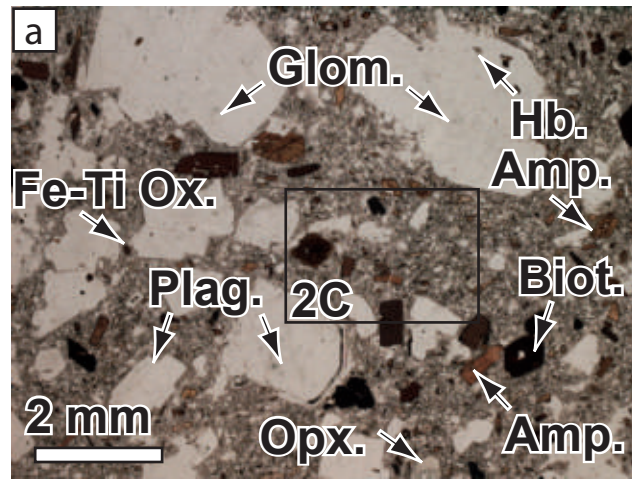
1024 Biotite; Gr.M.: groundmass; Plag.  $\mu$ L.: plagioclase microlites; Plag. Gl.: plagioclase glomerocrysts; W.R.: whole rock

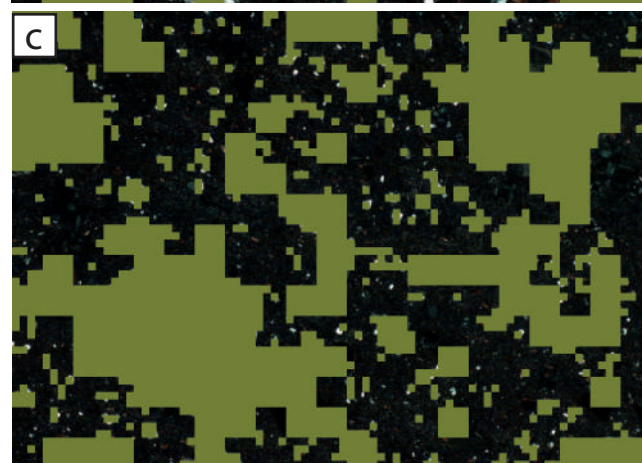
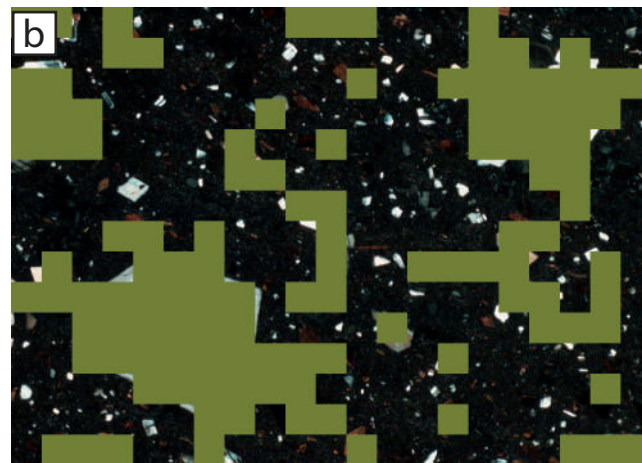
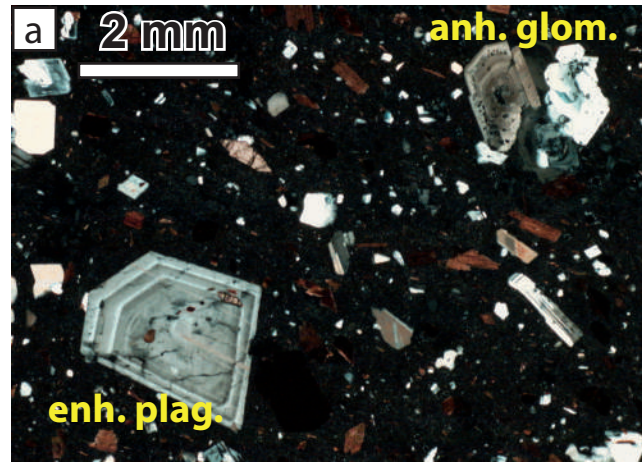
Sample code	Dated phase	Method	Fraction Size ( $\mu$ m)	K%	$^{40}\text{Ar}^* \pm 1\sigma$ (in % of total $^{40}\text{Ar}$ )		$^{40}\text{Ar}^*$ relative uncertainty	$^{40}\text{Ar}^* \pm 1\sigma$ $\times 10^{11}$ at/g		Age $\pm 1\sigma$ (in ka)		Weighted mean age $\pm 1\sigma$	
15CIO01	Amp.	S.S.	125-250	0.931	11.113	0.030	0.270%	13.85	0.037	1423	24		
					27.431	0.153	0.558%	13.34	0.074	1371	21	<b>1386</b>	<b>37</b>
15CIO01	Plag. Gl.	S.S.	125-250	0.822	7.353	0.053	0.721%	9.72	0.070	1132	24	<b>1132</b>	<b>24</b>
15CIO01	Biot.	S.S.	125-250	6.532	20.605	0.024	0.116%	38.88	0.045	570	9		
					16.920	0.029	0.171%	38.81	0.067	569	9	<b>569</b>	<b>9</b>
15CIO01	Gr.M.	S.S.	125-250	3.612	4.039	0.038	0.941%	7.70	0.072	204	6		
					3.874	0.056	1.446%	7.52	0.109	199	7	<b>202</b>	<b>6</b>
16CIO02	Plag. Gl.	S.S.	250-500	0.655	24.750	0.087	0.352%	12.66	0.044	1848	28	<b>1848</b>	<b>28</b>
16CIO02	Plag. $\mu$ L.	D.S.	63-125	0.654	7.503	0.036	0.480%	7.32	0.035	1071	21	<b>1071</b>	<b>21</b>
16CIO09	Plag. Gl.	S.S.	250-500	0.757	35.123	0.139	0.396%	7.55	0.030	955	14		
					35.222	0.114	0.324%	7.96	0.026	1007	15	<b>981</b>	<b>15</b>

16CIO09	Plag. $\mu$ L.	D.S.	63-125	1.714	6.101	0.039	0.639%	3.60	0.023	201	5	<b>201</b>	<b>5</b>
16CIO09	Biot.	S.S.	125-250	6.762	8.071	0.037	0.458%	13.87	0.064	196	4	<b>196</b>	<b>4</b>
16CIO08	Plag. $\mu$ L.	D.S.	63-125	1.568	4.834	0.031	0.641%	12.01	0.077	733	19		
					4.585	0.047	1.025%	12.19	0.125	744	21	<b>739</b>	<b>20</b>
16CIO04	Plag. $\mu$ L.	D.S.	63-125	1.104	1.422	0.039	2.742%	1.96	0.054	170	13		
					1.523	0.042	2.758%	1.84	0.051	160	12	<b>165</b>	<b>12</b>
15CIO09	W.R.	S.S.	40-500	2.119	7.907	0.120	1.518%	5.10	0.077	230	6		
					7.874	0.036	0.457%	5.11	0.023	231	5	<b>231</b>	<b>5</b>
15CIOX2	Biot.	S.S.	125-250	5.720	3.242	0.048	1.481%	33.54	0.497	561	21	<b>561</b>	<b>21</b>

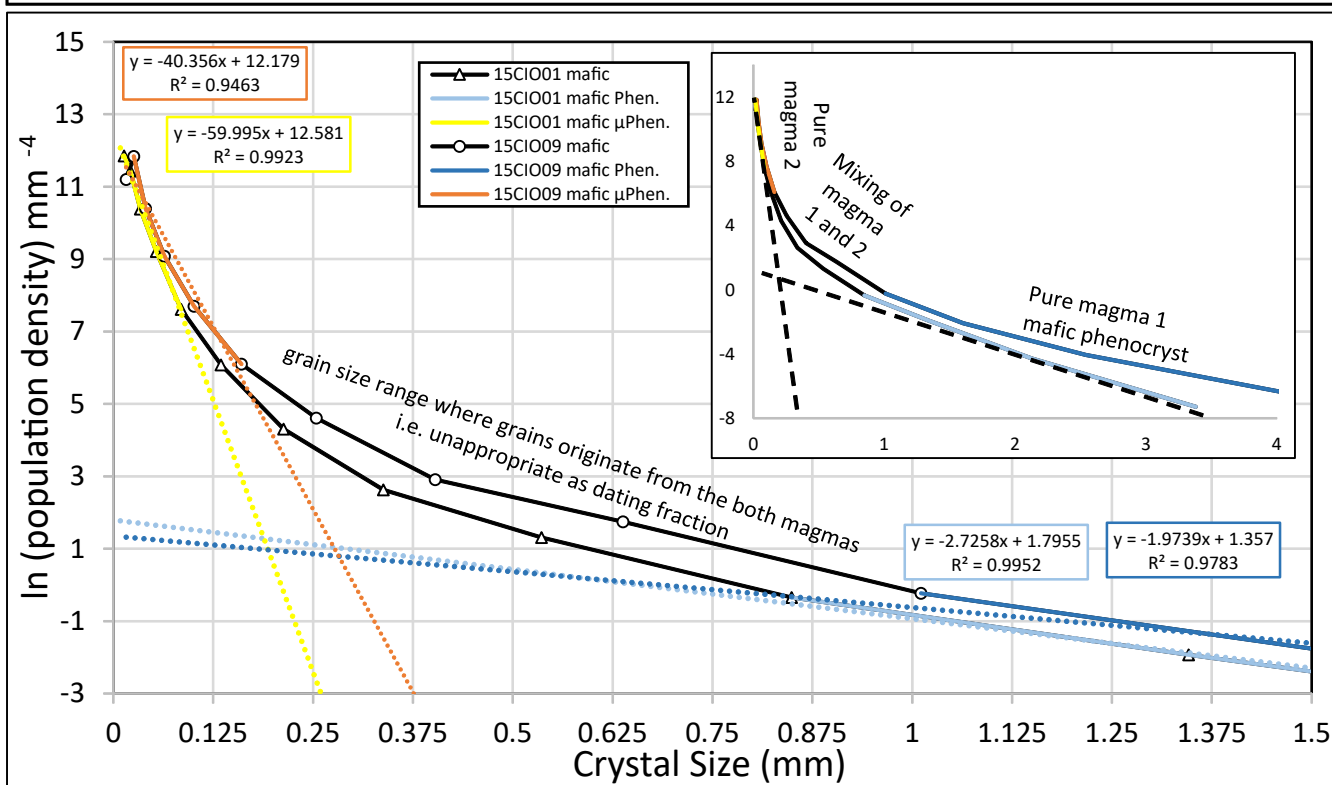
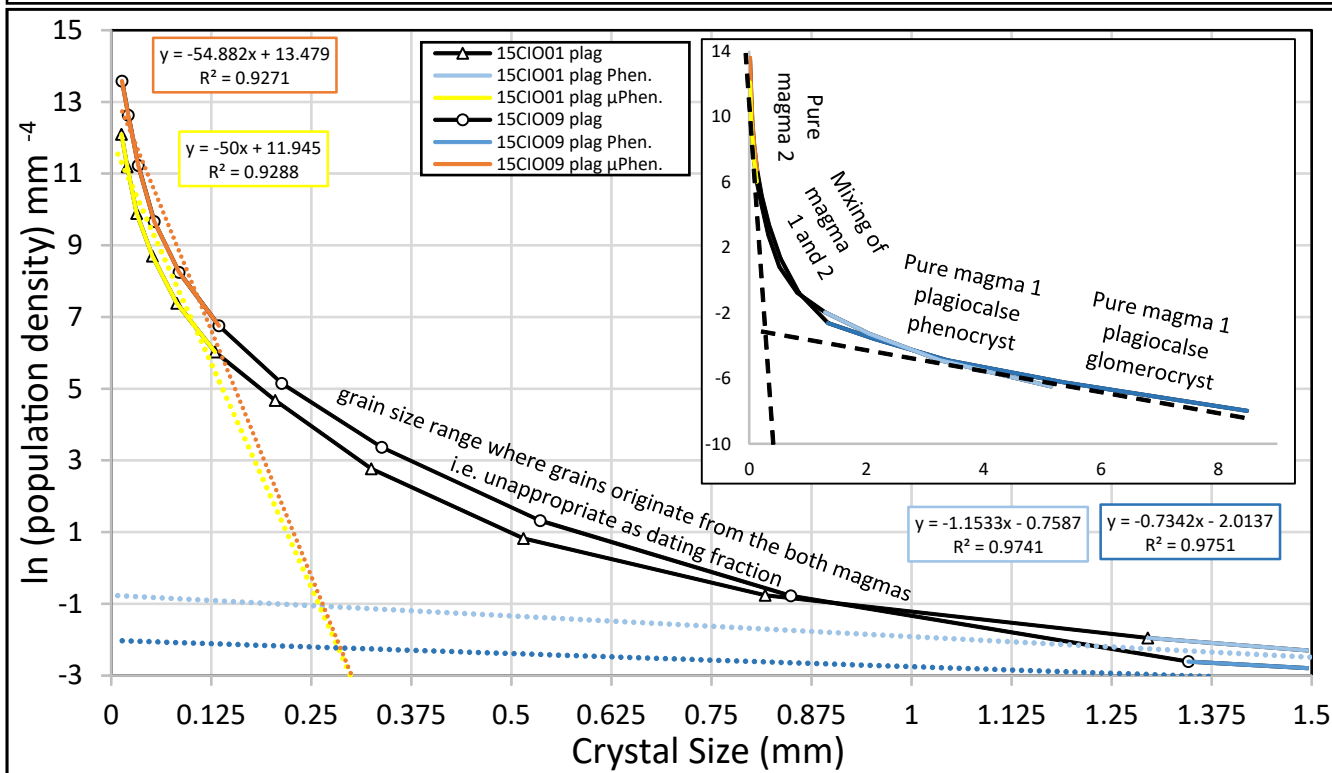
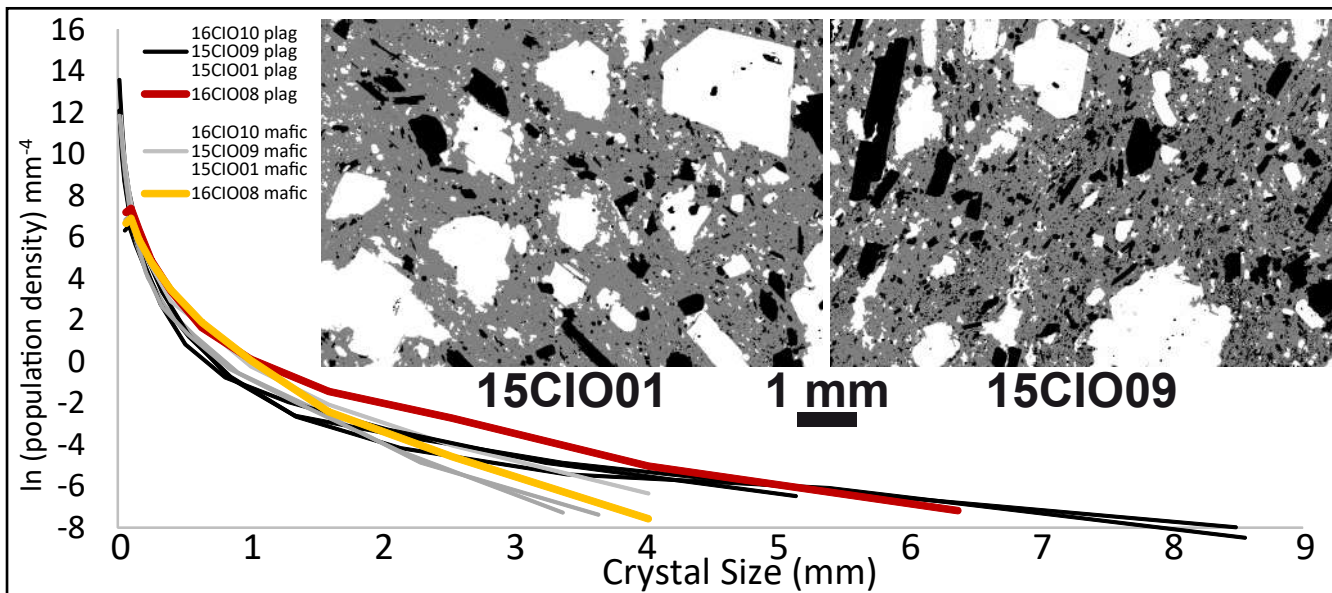
Figure\_01



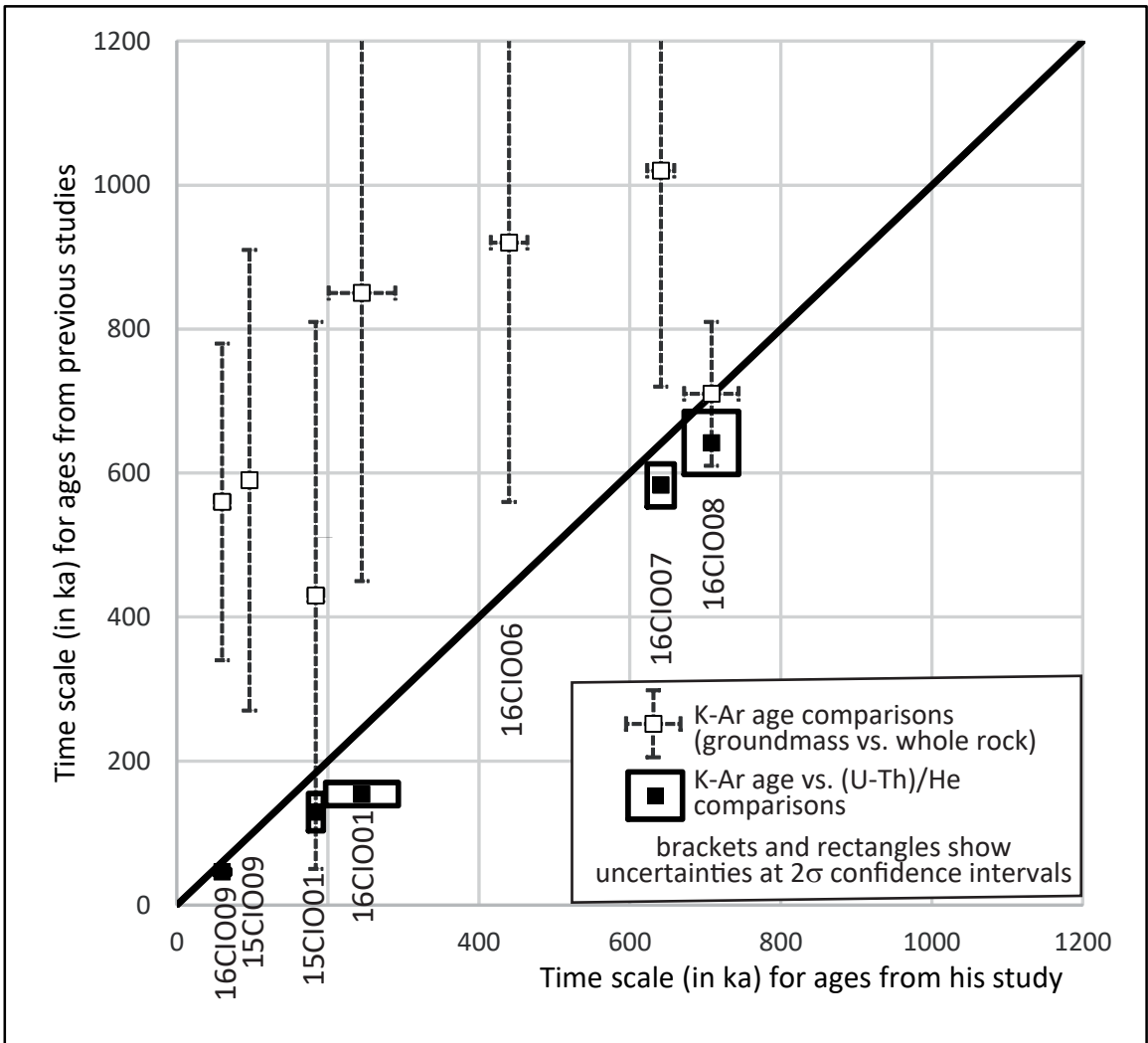




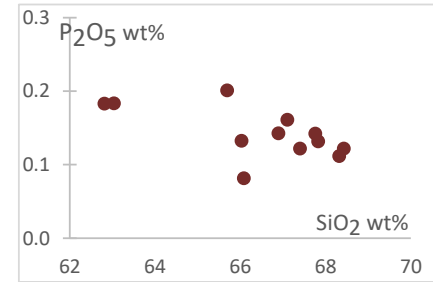
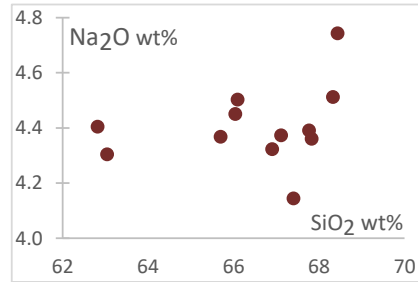
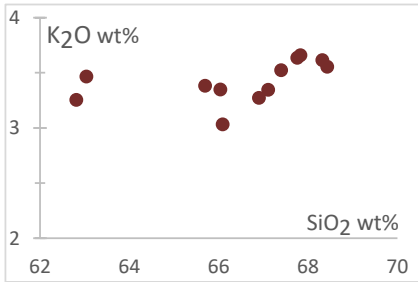
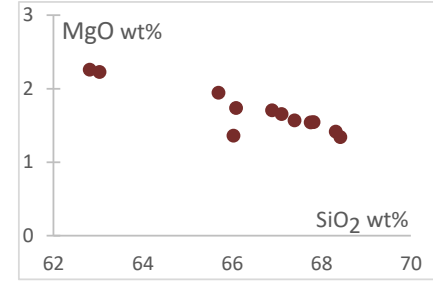
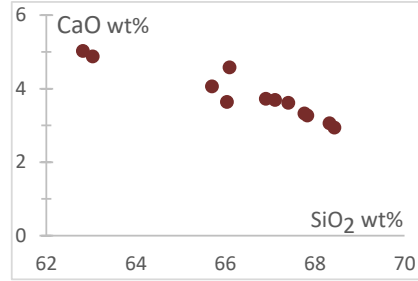
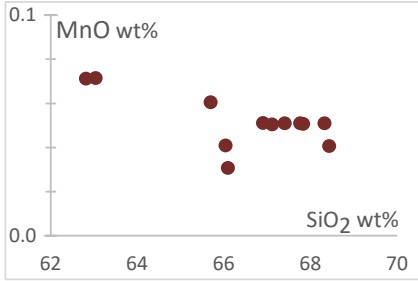
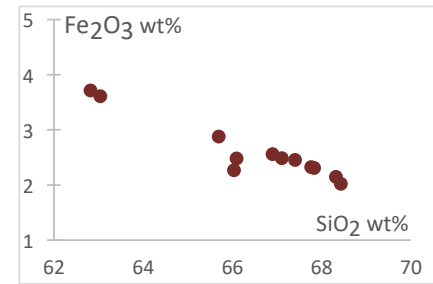
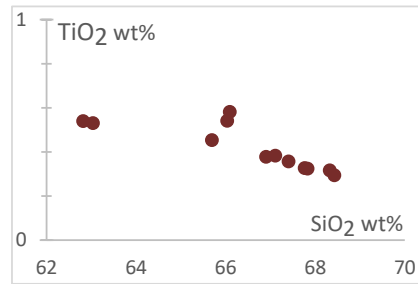
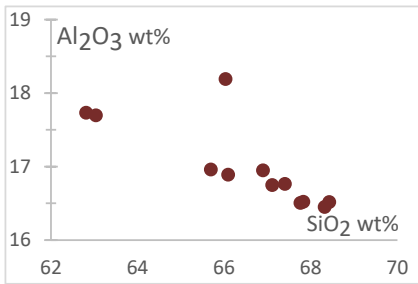
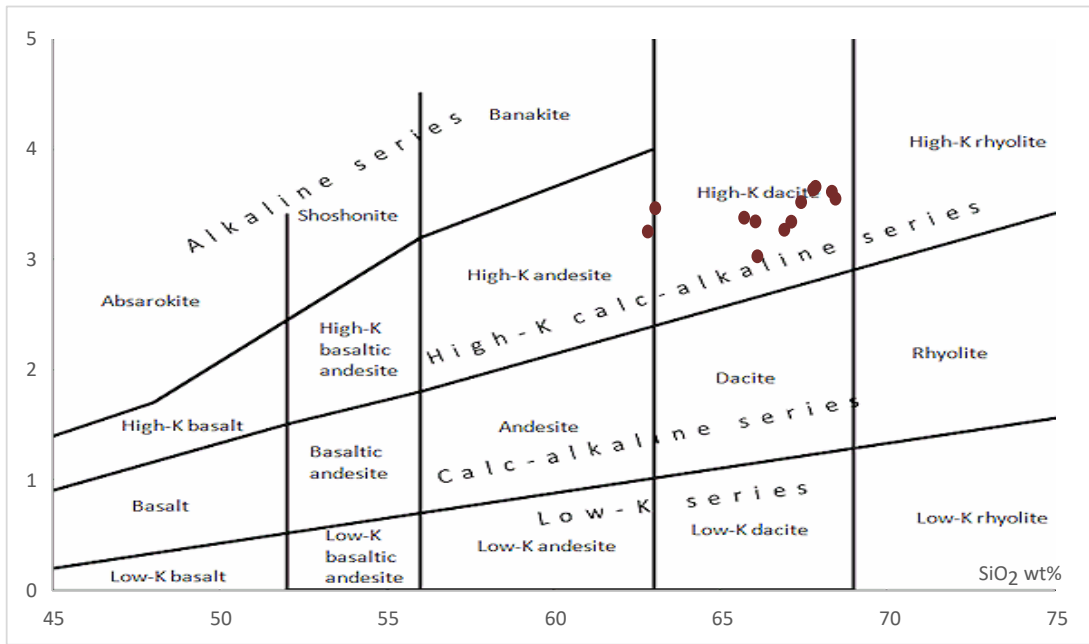
Figure\_04

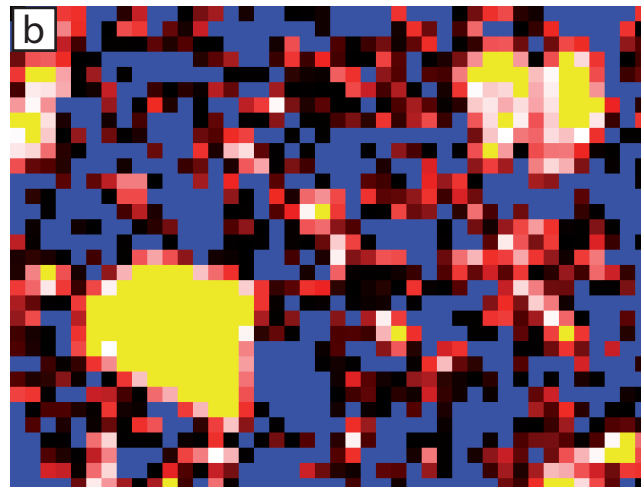
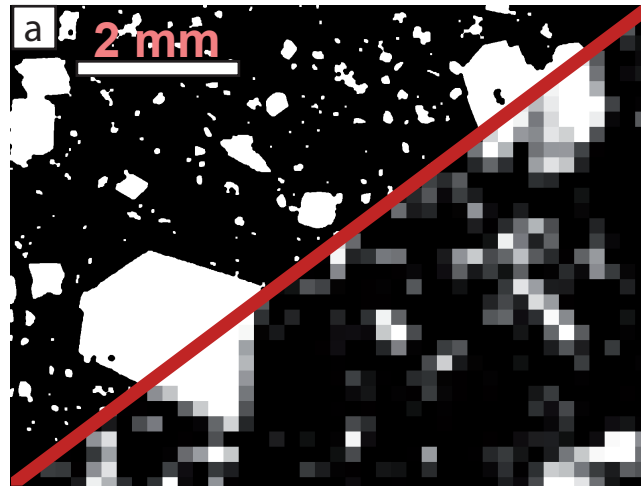


Figure\_05

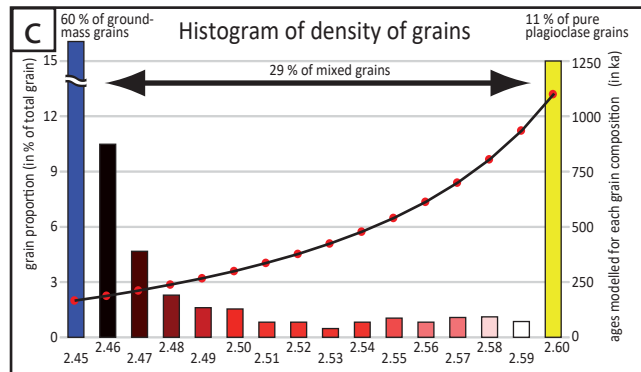


Figure\_06

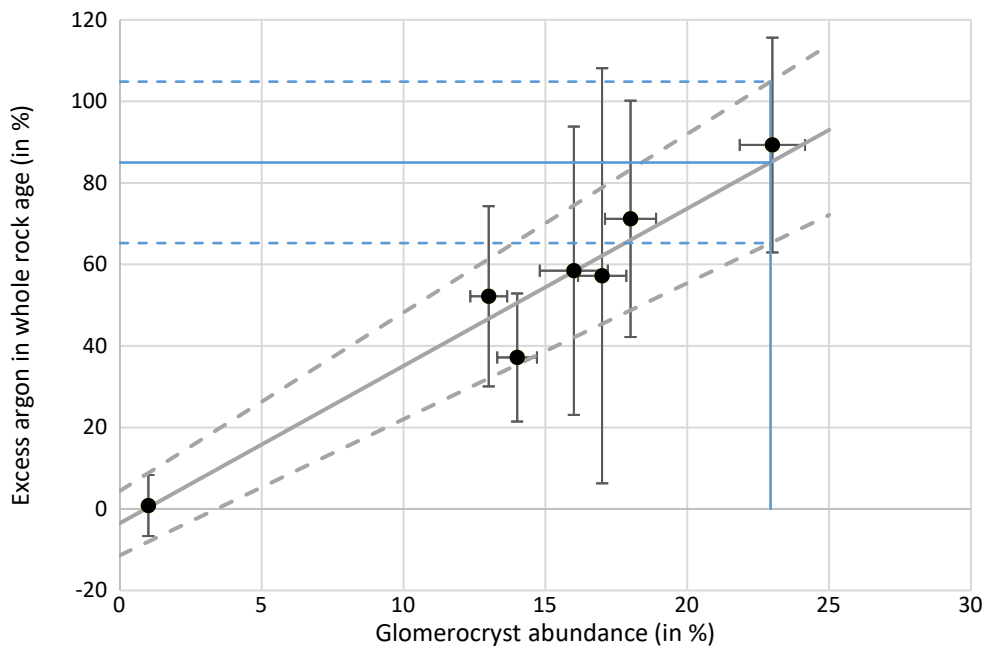




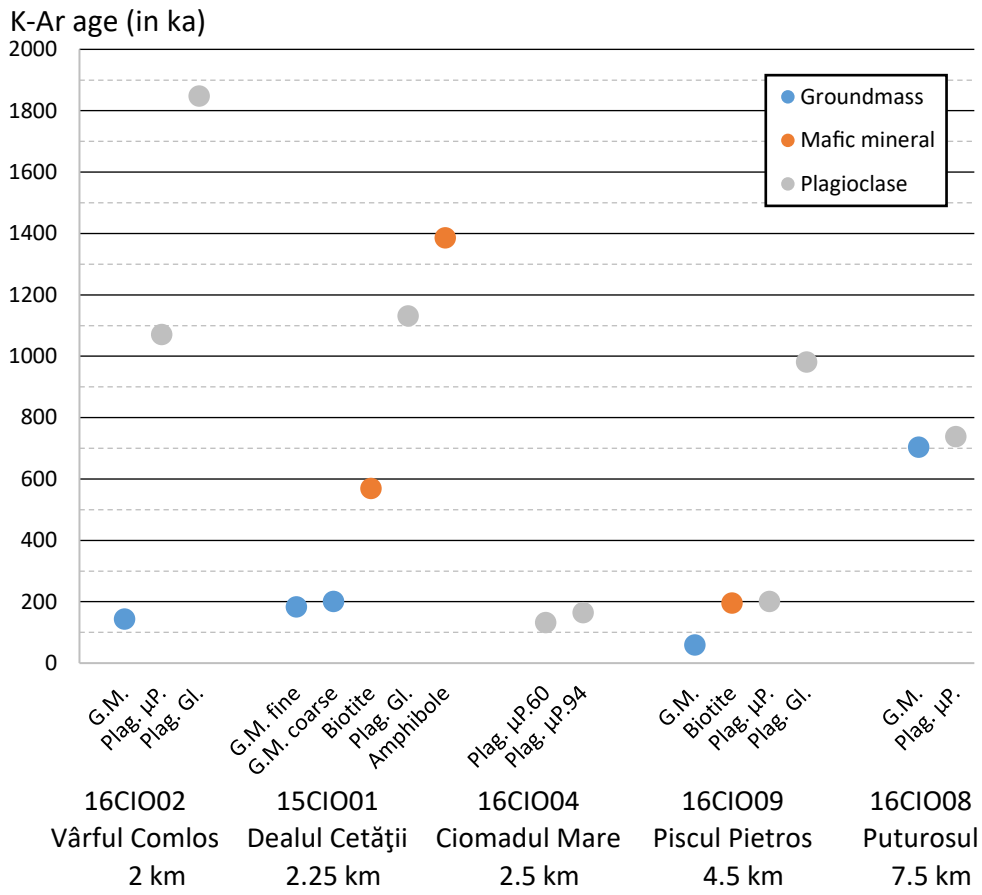
pure 184 ka groundmass grain      Mixed composition grain      pure 1.1 Ma plagioclase grain



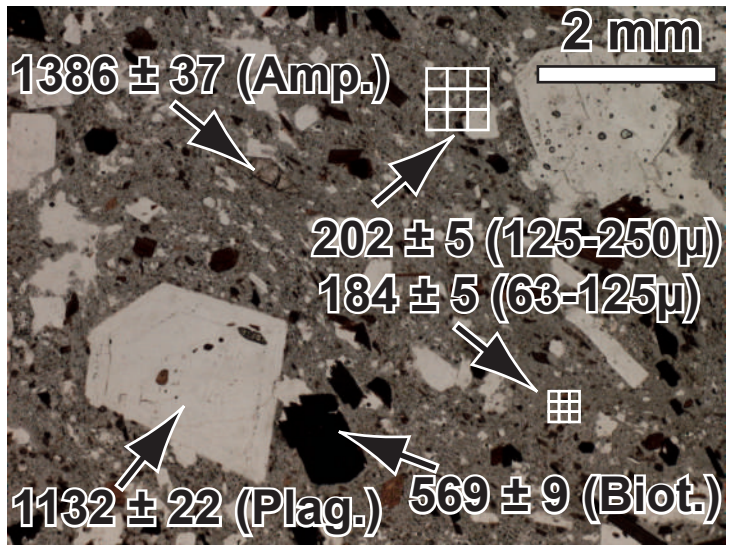
Figure\_08



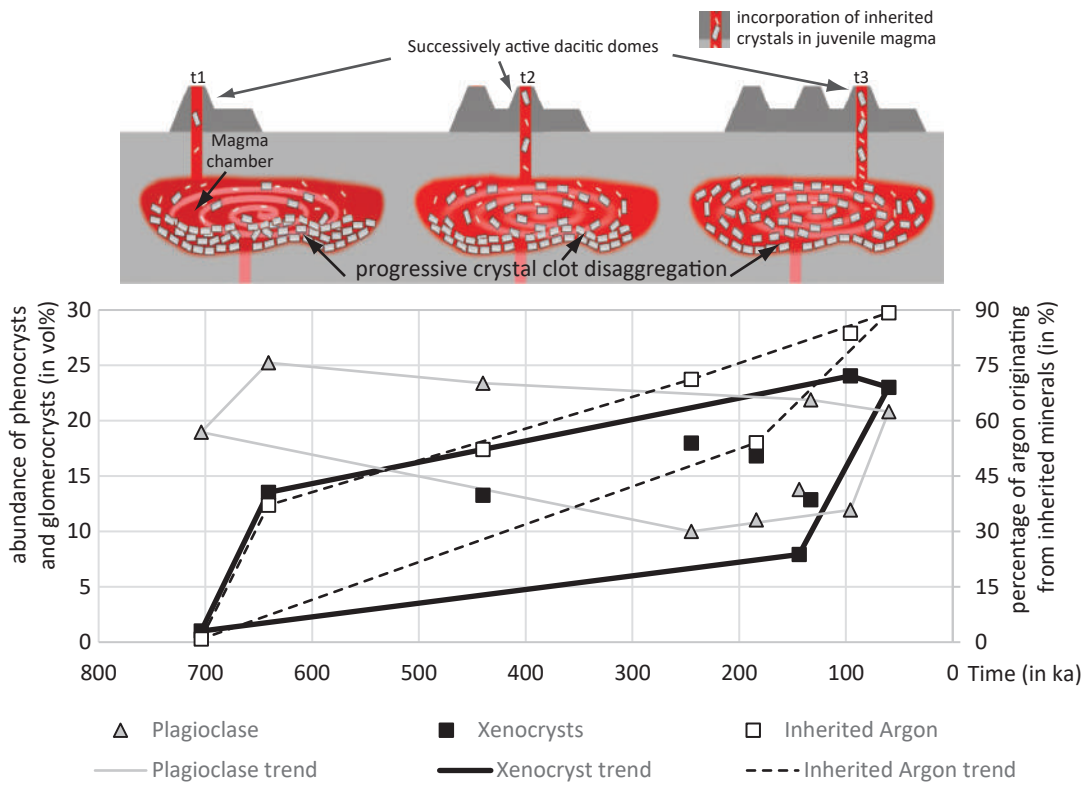
Figure\_09



Figure\_10



Figure\_11



Figure\_12

